# Observations of Shoaling Nonlinear Internal Bores Across the Central California Inner Shelf

Jacqueline M. McSweeney[1], James A. Lerczak[1], John A. Barth[1] , Johannes Becherer[1], John A. Colosi[2], Jennifer A. MacKinnon[3] , Jamie H. MacMahan[2], James N. Moum[1], Stephen D. Pierce[1], and Amy F. Waterhouse[3]

[1] College of Earth, Ocean, and Atmospheric Sciences, Oregon State University, Corvallis, Oregon, USA

[2] Department of Oceanography, Naval Postgraduate School, Monterey Bay, California

[3] Scripps Institution of Oceanography, University of California, San Diego, La Jolla, California

Corresponding author: Jacqueline McSweeney, jmcsweeney@coas.oregonstate.edu

***Accepted for publication at the Journal of Phiscal Oceanography***

**Abstract**

We present observations of shoaling nonlinear internal bores off the coast of central California. The dataset includes 15 moorings deployed September-October 2017 and cross-shore shipboard surveys. We describe the cross-shore structure and evolution of large-amplitude internal bores as they transit from 9km (100m depth) to 1km offshore (10m). We observe that two bores arrive each semidiurnal period, both propagating from the southwest and 72% of which are tracked to the 10m isobath. The bore speeds are subtidally modulated, but there is additional bore-to-bore speed variability that is unexplained by the upstream stratification. We quantify temporal and cross-shore variability of the waveguide (the background conditions bores propagate through) by calculating the linear longwave nonrotating phase speed ($c_o$) and using the nonlinearity coefficient of the Korteweg-de Vries equation ($\alpha$) as a metric for stratification. Bore fronts are generally steeper when $\alpha$ is positive and more rarefied when $\alpha$ is negative, and we observe the bore's leading edge to rarefy from a steep front when $\alpha$ is positive offshore and negative inshore. High-frequency $\alpha$ fluctuations, such as those nearshore driven by wind relaxations, contribute to bore-to-bore variability of the cross-shore evolution during similar subtidal waveguide conditions. We compare observed bore speeds to $c_o$ and the rotating group velocities ($c_g$), concluding that observed speeds are always faster than $c_g$ and are slower than $c_o$ at depths >32m and faster than $c_o$ at depths <32m. The bores maintain a steady speed while transiting into shallower water, contrary to linear estimates which predict bores to slow.

## 1. Introduction

Coastal internal waves (IWs) have piqued scientific interest since the 1960s (Perry and Schimke 1965; Cairns 1967; Lee 1961), resulting in a growing number of observational and modeling studies. They have been observed worldwide, including Massachusetts Bay (Chereskin 1983; Scotti et al. 2008; Thomas et al. 2016), the South China Sea (Alford et al. 2010; Li and Farmer 2011), Southern and Central California (Lerczak et al. 2003; Walter et al. 2012; Colosi et al. 2018), the Australian northwest shelf (Holloway et al. 1997), the Oregon coast (Stanton and Ostrovsky 1998; Moum et al. 2003), and the New Jersey shelf (Shroyer et al. 2011). These waves contribute substantially to transport and mixing on continental shelves.

Coastal IW research has encompassed a broad range of topics, including the generation, evolution, and destruction of high-frequency IWs (aka: solitary waves, solitons), internal bores, and the internal tide. The internal tide is an IW packet that is generated by the barotropic tide, has a long cross-shore length scale ~O(1-10km), and may include both bores and high-frequency IWs that are co-evolving. There is ongoing research related to the interactions of bores and high-frequency IWs, however this paper specifically focuses on the evolution of highly nonlinear, large-amplitude internal bores propagating across the shelf into shallower depths.

When the barotropic tide interacts with topography, such as the shelf break (Holloway et al. 1997) or a submarine bank (Lee and Beardsley 1974; Chereskin 1983; Scotti et al. 2007), it produces a large depression in the pycnocline. This depression wave propagates shoreward and evolves nonlinearly, with the leading edge steepening into a bore front (Lamb 1994; Scotti et al. 2007). Most observations indicate that one shoreward propagating bore is formed every semidiurnal ($M_2$) period (Chereskin 1983; Holloway 1987; Ramp et al. 2004; Scotti et al. 2007; Alford et al. 2010), but a handful of observations include two bores each semidiurnal period

(Lamb 1994; Shroyer et al. 2011). Since IWs facilitate significant cross-shelf exchange of energy and heat on the inner shelf, the presence of two $M_2$ bores likely has important dynamical and ecological impacts.

As an internal bore shoals, its evolution is influenced by its amplitude and the shelf stratification ahead of it (the upstream stratification). From the outer- to mid-shelf, an internal bore can propagate either as a single bore of depression or as an undular bore (Lee and Beardsley 1974; Chereskin 1983; Henyey and Hoering 1997; Apel 2003). As it transits into the inner shelf, the bore's evolution becomes strongly dependent on the upstream stratification (Helfrich et al. 1984; Vlasenko and Hutter 2002; Scotti et al. 2008). If the upstream pycnocline is above mid-depth, the bore's leading edge will continue to steepen and a sharp front will be maintained over the shoaling region. However, if the upstream pycnocline is near or below mid-depth, the bore's leading edge will rarefy, causing a decrease in the front steepness.

Several studies have used weakly-nonlinear theory to describe the waveguide (the background conditions a bore propagates through) by calculating the quadratic nonlinearity and dispersion coefficients, $\alpha$ and $\beta$, of the Korteweg-de Vries (KdV) equation (Helfrich et al. 1984; Holloway et al. 1997; Vlasenko and Stashchuk 2007; Shroyer et al. 2009). These studies draw attention to an important transition region during shoaling – the "critical depth" - where $\alpha$ changes sign, solitary IWs switch polarity (Shroyer et al. 2009), and a bore's leading edge may scatter into high-frequency waves (Helfrich et al. 1984). For a 2-layer system, $\alpha$'s sign suggests whether the pycnocline is above ($\alpha$ = +), at ($\alpha$ = 0, critical depth), or below mid-depth ($\alpha$ = -) (Grimshaw et al. 1997). An internal bore's cross-shore evolution depends on both 1) the upstream stratification, which can be described by $\alpha$ and may have local, high-frequency variability (Holloway et al. 1997; Vlasenko and Stashchuk 2007), and 2) the location of the

47 critical depth, which is not fixed. High-frequency fluctuations of $\alpha$, such as those caused by the
48 passage of an internal tide, can be especially impactful since nonlinearity is the dominant factor
49 controlling a shoaling bore's evolution (Scotti et al. 2008) and determining whether a bore will
50 break or develop a trailing packet of dispersive waves (Vlasenko and Hutter 2002).

51 While weakly-nonlinear theory provides valuable insight into shoaling IWs, most coastal
52 IWs are highly-nonlinear and thus our understanding of them necessitates models that are either
53 fully non-linear or incorporate higher-order nonlinearity. The extended KdV equation, for
54 example, includes a cubic nonlinearity term that becomes especially important to understanding
55 a wave's evolution when crossing the critical depth (Lamb and Yan 1996; Grimshaw et al. 1997,
56 2002; Lamb and Warn-Varnas 2015). Fully non-linear models that include rotation have also
57 demonstrated that both shoaling and rotation contribute to nonlinearities associated with the
58 decay and regeneration of wave packets (Helfrich 2007; Stastna et al. 2009; Grimshaw et al.
59 2014). This paper focuses on observational analyses and a comparison to linear bore speeds, but
60 we lean on findings from numerical studies to support our interpretation of these complicated,
61 nonlinear shoaling dynamics.

62 The evolution of an internal bore across the shelf and the location/isobath at which it
63 breaks has important implications for mixing and the cross-shelf exchange of water properties,
64 energy, and biota. For example, the shape of a bore's front during shoaling will determine
65 whether mixing is generated on the main pycnocline or near the bed (Moum et al. 2003; Shroyer
66 et al. 2010). Additionally, a bore's amplitude, speed, and evolving frontal shape will modify the
67 transport of particulates and nutrients, thus affecting the distribution and recruitment of various
68 littoral larval species (Pineda 1991, 1999; Scotti and Pineda 2004). These dynamical and

ecological impacts provide further motivation to understand drivers of waveguide variability and their influence on how internal bores evolve.

The 2017 Inner Shelf Dynamics Experiment (Lerczak et al. 2019) provides a unique and well-resolved dataset to study the propagation and evolution of internal bores from the mid (~100m depth) to inner (~10m) shelf of central California. Focusing on a region with roughly along-shore uniform bathymetry that shallows linearly to the coast, we quantify temporal (subtidal and bore-to-bore) and cross-shore variations in the waveguide by calculating $\alpha$ at 15 moorings. We also compare measured bore speeds to estimates of the linear longwave nonrotating phase speed and rotating group velocities, illustrating that bores do not slow over the shoaling region as predicted. We qualitatively describe how waveguide variations impact bore propagation, demonstrating that spatiotemporal variability in stratification strongly controls how bores evolve when transiting into shallower water.

## 2. Methods

We utilize a subset of the Inner Shelf Dynamics Experiment data (Lerczak et al. 2019) to focus on the region offshore of Oceano (Fig. 1), north of Pt. Sal, CA. The topography there is relatively planar, making the region well-suited for comparisons to two-dimensional theory.

### *a. Data Collection and Processing*

We analyze data from 15 moorings deployed in 100m-9m depth from September 6, 2017 to October 31, 2017 (Fig. 1). Several moorings were serviced October 5-8, 2017.

Each lander mooring (Fig 1, "A") had a tripod with an upward looking ADCP that was connected to a surface buoy. These had temperature sensors on the tripod and surface buoy, but

92 no instrumentation mid-watercolumn. The string moorings (Fig 1, "T") had primarily
93 temperature loggers at roughly 1-2m increments and were kept taut by two subsurface buoys
94 (~2m and 5m below the surface). Using pressure sensors distributed vertically on the MS100
95 and OC50 moorings, we estimate that mooring tilt contributed to a vertical displacement of 2-
96 15cm over a tidal cycle. For locations with both a lander and string mooring, the two were
97 deployed with a horizontal separation of ~1 water depth.
98 Temperature was the dominant control on density during the experiment, with salinity at
99 the OC50 ranging from 33.25-33.58 g/kg over the entire observational period. Thus, density is
100 calculated assuming a constant salinity of 33.43 g/kg at all moorings.
101 Data processing included extrapolation of velocity, temperature, and density data to the
102 surface and bed. Velocity data is missing in the ~10% top part of the water column due to side
103 lobe contamination and from the bed to ~1.5 meters above the bed (mab). Temperature loggers
104 were deployed from ~0.5 mab and to ~0.5-2m below the surface. Both velocity and temperature
105 measurements were extrapolated using a quadratic polynomial regression and assuming no-shear
106 at the boundaries. After extrapolation, temporal gaps <5 min were filled using linear
107 interpolation. All temperature and velocity data were averaged to 1min resolution
108 Lamb (2002) demonstrated that properties of large-amplitude IWs, such as those
109 observed here, are sensitive to near-surface stratification. Given the lack of surface data, wave
110 properties estimated from stratification may be sensitive to the extrapolation methods. A few
111 moorings had surface-following temperature sensors, so we used these to confirm that calculated
112 wave properties were minimally influenced by our surface extrapolation methods.
113 Shipboard surveys were conducted from the R/V Oceanus September 6-17, 2017. We
114 present six cross-shore transects along the southern-Oceano mooring line on September 9$^{th}$ that

115 captured the cross-shore propagation of an internal bore (Fig. 1). During this survey, the ship
116 steamed at ~3 knots while towyo-ing a CTD package, yielding a resolution of ~200m
117 horizontally and ~0.1m vertically. Shipboard velocity data collected from a downward-looking
118 pole-mounted 600-kHz ADCP with 1m bins were ensemble averaged to 1-min.
119 Survey transects were converted to cross-shore distance using a shoreline reference (Fig.
120 1, small red dot). Temperature measurements were interpolated to this coordinate system using a
121 2D-LOESS filter with decorrelation scales of 250m (horizontal) and 0.25m (vertical). Velocity
122 data were transformed to a north-east reference frame and used to identify the bore fronts for
123 speed estimates (section 3.a). The 1min-averaged velocity data were then further smoothed using
124 the same 2D-LOESS filter.
125
126 *b. Data Analysis*
127 1) Quantifying Background Stratification
128 Inner shelf stratification is influenced by interacting processes on a broad range of
129 spatiotemporal scales, including mesoscale/submesoscale eddies and winds. To study how
130 stratification variability influences internal bores, it is necessary to identify the background
131 stratification through which the bores propagate. However, this is challenging because internal
132 bores themselves, which are persistently present on the shelf, significantly modify shelf
133 stratification. It is not obvious how to objectively define the background stratification, and we
134 find that a simple, time-averaged density field is not representative of the environment IWs
135 actually encounter. To address these nuances, we calculate the background density in two ways
136 and compare their influences.

137 The first method of estimating background density, termed "sorted density" onward,
138 focuses on capturing subtidal variability at each mooring. Following a method similar to that
139 used by Winters et al. (1995), we sort all density measurements, uniformly spaced in depth,
140 within 24.84 hrs (twice the M2 period) by increasing value, and scale this density profile to the
141 total depth. This is done for the entire timeseries with a 6hr moving-window. This method
142 assumes that IWs are simply displacing isopycnals, thus minimizing the influence of IWs and
143 focusing on the modulation of stratification by subtidal processes.

144 Our second estimate, termed "pre-arrival density", describes the local stratification just
145 prior to a bore arrival. Using arrival times (section 2.b.2), we compute the 30-minute average
146 density profile before each bore's arrival.

147 We use these two density products to additionally calculate the quadratic nonlinearity
148 KdV coefficient ($\alpha$), which we utilize as a metric of stratification for this analysis. The KdV
149 equation, which is described thoroughly in Grimshaw et al. (2004), relates changes in the vertical
150 displacement of the pycnocline, $\eta$, to nonlinearity and dispersion in the absence of rotation:

151 $$\frac{\partial \eta}{\partial t} + (c_o + \alpha\eta)\frac{\partial \eta}{\partial x} + \beta\frac{\partial^3 \eta}{\partial x^3} = 0 \qquad (1)$$

152 where, $c_o$ is the mode-one longwave linear phase speed, $\beta$ is the dispersion coefficient, $x$ is the
153 cross-shore horizontal coordinate, $t$ is time, and $\eta$ varies in both $x$ and $t$. In the absence of
154 background shear, the nonlinearity and dispersion coefficients are:

155 $$\alpha = \frac{3\int_{-H}^{0} c_o^2 \left(\frac{\partial \phi}{\partial z}\right)^3 dz}{2\int_{-H}^{0} c_o \left(\frac{\partial \phi}{\partial z}\right)^2 dz} \quad \text{and} \quad \beta = \frac{\int_{-H}^{0} c_o^2 \phi^2 dz}{2\int_{-H}^{0} c_o \left(\frac{\partial \phi}{\partial z}\right)^2 dz} \qquad (2)$$

where $\phi$ is the vertical structure function, z denotes the vertical coordinate system, and $H$ is the total water depth.

It is well known that background shear can significantly influence the propagation and evolution of a shoaling bore (Lee and Beardsley 1974; Stastna and Lamb 2002), but we intentionally exclude shear in our estimates of $\alpha$ and $c_o$ to focus on the influences of stratification. This decision is motivated by our finding that $\alpha$ and $c_o$ estimates are sensitive to the definition of background shear and, like the background stratification, this choice is not obvious. While shear and stratification both play a role in modulating IW characteristics, their relative influences cannot be delineated in a simple way. Other IW studies have excluded shear to strategically elucidate effects of stratification (Holloway et al. 1997; Scotti et al. 2007), and we similarly do so with the intention of discussing shear impacts in a follow up paper.

2) Identifying Internal Bore Arrivals

To discuss the evolution of shoaling internal bores, we must track a bore as it transits through the mooring array. We do so using the following methods:

First, we identify all bore arrivals at each mooring using a filtered pycnocline displacement. We select an isopycnal that qualitatively tracks the pycnocline and calculate its displacement ($Z_p$) relative to its background depth from the sorted density profile. Because the background stratification evolves over the 2 months, a single isopycnal is not representative of the pycnocline for the whole timeseries. Thus, we conduct this analysis with three isopycnals and choose the most representative of the pycnocline at a given time. To identify an arrival, we bandpass filter (0.5-16 hour) the isopycnal displacements and find local minima of $\frac{dZ_p}{dt}$. This

approach targets instances in the semidiurnal period in which the pycnocline is rapidly displaced downwards. Stratification and IW conditions impact the magnitude/rate of displacement, so we cannot place thresholds on how far/fast the pycnocline must be depressed to qualify as a bore. Thus, local minima are identified automatically and we use the 1-min temperature and eastward semidiurnal velocity data to manually confirm that the minima coincide with a bore's passage. From this step, we quantify the number of bores observed at each mooring (Table 1, column 2).

The second step is to track each bore as it transits through the array. This involves comparing the arrival times at neighboring moorings over the period a shoreward-propagating wave would arrive (assuming 0.2 – 0.7m/s speeds) and tracking specific features of both the bore and high-frequency IWs using the 1-min temperature data, band-passed (3min-16 hour) eastward velocities, and 0.5-16hr pycnocline displacements. This step-2 product, termed "tracked bores", includes 148 bores at MS100, the majority of which are observable to shore (Table 1, column 6).

The final step is to flag tracked bores by the certainty associated with their arrival times (Table 1, column 7-8). Informed by an analysis of the error in speed estimates associated with arrival time uncertainty (section 2.b.4), we select certainty thresholds of +/-7.5 and +/-15 minutes. For example, a sharp bore with a pycnocline displacement of 25m within 2 minutes would be positively flagged for the +/-7.5 min threshold. However, a bore with a gradually-sloped leading edge that displaces the pycnocline 30m over 25 mins would be flagged only under the +/-15min threshold. Note that the threshold is +/- minutes from a centered arrival time, so the window of certainty is double the threshold value.

Bores are much easier to track when the leading edge is steep (compared to more rarefied). Thus, steps 1 and 3 likely contribute to an underestimation of the bores with gently-sloped fronts.

201

202 3) Calculation of Bore Speed and Direction

203 We estimate the propagation direction and speed of each bore using arrival times at
204 various mooring groups, following Scotti et al. (2005) and Thomas et al. (2016). This method
205 assumes that a bore propagates through a mooring group as a straight linear feature with constant
206 speed and direction. Speed and direction are estimated by minimizing the root-mean-square
207 difference in observed arrival times at each location and the arrival time predicted for a particular
208 speed/direction.

209 Mooring groups include both triangles and rectangles (Fig. 1). For example, triangle A
210 consists of OC50, OC40N, and OC40S, yielding a speed/angle midway between the 50 and 40m
211 isobaths, while square B uses OC40N, OC40S, OC32N, and OC32S to yield estimates between
212 the 32 and 40m. For the rectangles, we average the speeds estimates from each possible triangle.
213 This permits an estimate when a bore is observed at only 3 moorings, increasing the number of
214 estimates. We compute speeds using only bores flagged by the +/15 min certainty, so there are
215 fewer speed estimates (Table 2) than tracked bores (Table 1).

216 We then calculate linear speeds from both density products using the following
217 eigenvalue problem:

218
$$\frac{\partial^2 \phi}{\partial z^2} + \frac{1}{c_o^{\,2}} \frac{N^2}{\left(1 - \frac{f}{\omega}\right)} \phi = 0 \tag{3}$$

219
$$c_o = \frac{\omega}{k} \tag{4}$$

220
$$c_g = \frac{\partial \omega}{\partial k} \tag{5}$$

where, $N^2$ is the squared buoyancy frequency, ω is frequency, $f$ is the Coriolis parameter, and $k$ is the wavenumber. Given our decision to exclude shear in the this analysis (section 2.b.1), Equation 3 is for a case without background current. We calculate $c_o$ for the nonrotating case ($f$ = 0) and the group velocities, $c_g$, for the rotating case with ω=12.42 hrs. For the remainder of the paper, $c_o$ denotes the nonrotating phase speed.

4) Estimating Error in Bore Speed/Direction Calculations

To determine the error associated with the speed estimates from the triangulation method, we conduct an error analysis using synthetic IWs of known speed and direction. We run 8 cases – 4 for both triangle A and D, with waves speeds of 0.1, 0.15, 0.2, and 0.25 m/s – and each case includes 10,000 synthetic waves (Fig. 2). For each wave, the propagation direction is assigned randomly and random error scaled by a standard deviation ranging from 0-22.5 mins is introduced to the arrival time estimates. Estimates of speed/direction from the triangulation method are compared to known values. We conclude that speed estimates are more accurate offshore (triangle A) than nearshore (D) and improve as the waves slow down. For arrival times with a certainty of +/- 7.5 minutes, the speed estimate of a 0.25m/s bore at triangle A is within 0.035 m/s of the true speed and the wave direction is within 8°. Comparatively, a bore of the same speed with a certainty +/15 minutes would have a speed/angle estimate that is within 0.07m/s and 16° of the true values.

## 3. Results

### *a. The Cross-Shelf Structure of the Internal Bores*

During the 7-hour ship survey, we track a large-amplitude internal bore from 7.7 km (51.6m depth) to 2.2 km (24.5m depth) offshore (Fig. 3). The bore front remains sharp during

244 the entire transit to shore. If we consider the bore to be 2-layered and the 13°C isotherm a proxy
245 for the pycnocline boundary, we can estimate the bore's amplitude relative to the total water
246 depth (Table 3). Notably, the bore's amplitude is roughly half the water depth across the entire
247 transect.

248 We estimate the bore speed from the distance traveled between front passages (Fig. 3
249 black text). Errors in this calculation are estimated by adding +/- 2 minutes of error to the
250 passage times. For example, the error for the speed between t=0 and t=1.3hr is estimated from
251 the difference between the speeds calculated from time/distance measurements at $t_0$ and $t_{1.3hr}$ and
252 from those at ($t_0$-2mins) and ($t_{1.3hr}$ + 2mins). The bore remains a fairly constant speed as it
253 propagates to shore. In contrast, the estimate of $c_o$ estimated from the sorted density from nearby
254 moorings (Fig. 3, grey text) predicts the bore to significantly slow over this shoaling region.

255 Considering each cross-section to be a "snap-shot" of the bore, the conditions prior to the
256 bore arrival are characterized by offshore flow in the stratified surface layer compensated by
257 shoreward flow at depth. There is a sharp depression of the pycnocline at the bore's leading
258 edge followed strong onshore velocities at the surface and offshore velocities in the lower layer.
259 The currents associated with the bore weaken as the bore transits into shallower water.

260 We compare the survey-view of the bore (Fig. 3) to observations from the southern cross-
261 shore mooring transect (Fig. 4). Similarly, we observe a sharp bore front (Fig. 4, green triangles)
262 that can be tracked from the 100m isobath to 9m and depresses the pycnocline by roughly half
263 the water column depth at all locations (except MS100). After the front passage, there is a
264 surface, shoreward current compensated by off-shore flow at depth. These currents are weaker
265 inshore compared to offshore, consistent with the survey data. Observed bore speeds corroborate
266 that the bore maintains a steady speed while shoaling. These timeseries also offer insight into

267 the bore's high-frequency structure, which isn't captured by the ship survey. For example, there
268 are high-frequency elevation waves following the bore front at OC32S that have mostly
269 disappeared by OC25SB.
270
271 *b. Observation of Two Internal Bores within a Semidiurnal Period*
272 Bores transiting shoreward through the mooring array are evident in a 2-day timeseries of
273 east-west velocity and temperature from the northern cross-shore mooring transect (Fig. 5).
274 Focusing on MS100, we observe a bore arrival at the 100m isobath roughly every 6 hours (9
275 bores over the 52 hour period), all of which are trackable to shore.
276 Over the observational period that includes data from OC10N, 86 bores are observed at
277 the 100m and 50m isobaths. 90% of these can be tracked to the 25m isobath, 81% to 17m, and
278 72% to 10m. However, if we consider only arrival that meet +/- 15min certainty threshold, 62%
279 are trackable to 25m, 55% to 17m, and 45% to 10m. Bores onshore of the 25m isobath are
280 harder to identify due to the evolution of the bores' leading edge, and thus this estimate of bores
281 that make it to shore is likely an underestimate.
282 We plot histograms of the number of hours between subsequent bores across the northern
283 shoaling region, excluding cases where $\Delta t > 24$hr (Fig 6). These histograms confirm a peak at
284 ~6-7 hours for all moorings, though the peaks are broader at moorings shallower than 40m. This
285 suggests that there are times when bores don't propagate all the way to shore and other times that
286 two bores within a semidiurnal period are observed at the inshore locations.
287 The arrival of two bores each semidiurnal period is a surprising finding (section 4.a), but
288 given this observation, we use it to estimate the maximum number of expected bores. If two

289 bores arrived every semidiurnal period for 53 days (the observational period), 212 bores would
290 be expected. Thus, we observe 84% of the maximum number of potential bores at MS100.
291
292 *c. Stratification Variability*
293 To discuss spatiotemporal variability of the waveguide, we consider the upstream
294 stratification conditions at the northern cross-shore mooring line. We compare the subtidal and
295 pre-arrival density fields, as well as their corresponding $\alpha$ estimates.
296 Timeseries of sorted densities illustrate that the stratification conditions had considerable
297 subtidal variability and across-shore structure during the observational period (Fig. 7). In
298 early/mid-September, warm surface temperatures ~O(17°C midshelf to 18.5°C inner shelf)
299 contributed to a relatively strong vertical stratification and horizontal cross-shore density
300 gradients. For example, on September 13 the surface waters were more dense at OC40 than at
301 both MS100 and OC17N, and the pycnocline was well above mid-depth offshore at MS100 but
302 less defined inshore at OC17N. Comparatively, in late September/early October vertical
303 stratification weakened, the pycnocline was less defined, and the horizontal cross-shore density
304 gradients were less pronounced.
305 The subtidal stratification does not capture the specific stratification an individual bore
306 propagates through (Fig. 7), especially since bores travel through the region roughly every 6
307 hours and influence the stratification ahead of the next bore. To assess the importance of local
308 upstream stratification, we compare the sorted and pre-arrival densities at OC50 (Fig. 8). The
309 subtidal features are qualitatively similar in both density products, but the pre-arrival data
310 illustrate higher-frequency variability in the vertical density structure, which impacts $\alpha$ and $c_o$.
311 For example, during early/mid-September when stratification is strong, there is heaving of the

312 isopycnals ~O(10m), 1/5 the water depth, on timescales shorter than a day which cause relatively
313 large fluctuations in $\alpha$.

314 To understand the broader context of the observed subtidal stratification variability, we
315 present a timeseries of $\alpha$ estimated from the sorted density at the northern moorings along with
316 the subtidal wind and the timing of bore arrivals relative to the barotropic tide (Fig. 9). We note
317 that the observational period spans several spring-neap cycles and roughly 7 wind-relaxations.
318 Without distinguishing how these two timescales and physical processes may contribute
319 differently to subtidal variability, we observe a strong subtidal modulation of $\alpha$ over the
320 observational period. The subtidal modulation of $\alpha$ at MS100 is quite distinct from that at the
321 shallower moorings and will be discussed further in section 4.b.

322 The cross-shore variability of $\alpha$ is indicative of important cross-shore gradients in the
323 waveguide (Fig. 9e). While $\alpha$ at MS100 is always positive, its sign at the other moorings
324 oscillates. Values of $\alpha$ at OC50 and OC40N are strongly correlated, as are those at OC25NA
325 and OC17N. In general, the magnitude of $\alpha$ decreases from offshore to nearshore, but the
326 oscillations are higher frequency and larger magnitude at the shallowest locations. The
327 differences between OC50/40N and OC25NA/17N indicate that these two cross-shore regions
328 are dynamically distinct.

329 A comparison of the subtidal, offshore wind (>33hrs) and $\alpha$ at the individual moorings
330 confirms that stratification in the nearshore ($\leq$ 25m depth) is highly-correlated with wind (Table
331 4). Lagged negative correlation coefficients between $\alpha$ and subtidal winds are less than 0.05 for
332 the isobaths 40m and deeper, but are ~0.2-0.28 for the 25, 17, and 10m isobaths. The time lags
333 range from 1-3 hours. From the lagged timeseries comparison of subtidal wind and -$\alpha$ at these

334 shallower moorings, it appears that the nearshore response to changes in the offshore wind is not
335 always consistent (Fig. 10).

336 Bore-to-bore variability in $\alpha$ is clear from the pre-arrival estimate, indicating higher-
337 frequency variability of the upstream waveguide (Fig. 8). The pre-arrival $\alpha$ is often larger than
338 that estimated from sorted stratification, which is consistent with observations of the pycnocline
339 upheaving prior to a bore's arrival (Figs. 4 and 5). These nuances illustrate the sensitivity of $\alpha$ to
340 how the background density profile is defined.

341

342 *d. Internal Bore Characteristics*

343 1) Qualitative differences in the bores during different subtidal conditions

344 An order one question is whether the internal bores are qualitatively different when $\alpha$ is
345 positive, negative, and near-zero across the shoaling region. To answer this question, we identify
346 3 time periods when the cross-shore gradient of subtidal $\alpha$ is different (Fig. 9 grey shading): 1) $\alpha$
347 is positive across the shoaling region, 2) $\alpha$ is positive offshore and negative inshore, and 3) the
348 subtidal $\alpha$ is near-zero at locations $\leq$50m depth.

349 Comparing 2-day timeseries at the northern cross-shore mooring transect (Fig. 5, 11, 12),
350 it is clear that the IW field is quite distinct during these 3 periods. Bores are trackable to shore
351 over the entire observational period (Fig. 9b), but sharp bore fronts are most often observed
352 when $\alpha$ is positive. The depth-averaged semidiurnal kinetic energy ( $\overline{KE_{SD}}$ ) at each mooring
353 varies within the observational period (Fig. 9c), which also must be considered when comparing
354 the three $\alpha$ regimes. Specifically, at the 100m and 50m isobaths $\overline{KE_{SD}}$ increases over the
355 observational period whereas at the 25m mooring it decreases from September to October. This

356 implies that cross-shore gradients in $\overline{KE_{SD}}$ are changing significantly during the experiment. We
357 focus on linking cross-shore gradients of $\alpha$ to qualitative differences in the internal bore
358 evolution, but will further discuss the waveguide as it relates to kinetic energy in section 4.b.
359 When $\alpha$ is positive across the shoaling region (Fig. 5), the leading edge of the bores have
360 a sharp front that is sustained across the inner shelf. The bores are easily trackable to shore, and
361 there is little to no rarefication of the bores' leading edge. The bores are large amplitude, and the
362 pycnocline is depressed quickly downwards with each bore arrival. After the bore front passes,
363 the pycnocline relaxes relatively slowly to the pre-bore position. In cases where the pycnocline
364 is still somewhat depressed when the next bore arrives, the subsequent bore encounters different
365 $\alpha$ conditions and the pre-arrival stratification is likely more important than the subtidal $\alpha$.
366 The bore fronts are more rarefied $\alpha$ is negative, leading to increased difficulty tracking
367 them all the way to shore when $\alpha$ nearshore is negative (Fig. 11). Though subtidal $\alpha$ at OC50 is
368 near-zero, the pre-arrival $\alpha$ is positive (Fig. 8) which explains why the bores at OC50 look
369 qualitatively similar to the period when $\alpha$ is positive at locations (Fig. 5). From the 40m isobath
370 and shallower, there is greater variability in $\alpha$ immediately prior to a bore's arrival which leads a
371 range of bore shapes. For example, at OC32N the majority of the bores encounter a negative $\alpha$
372 and have a rarefied leading edge, but the bore that arrives September 23 22:15 has a positive
373 upstream $\alpha$ and a sharp leading edge (Fig 11).
374 When subtidal $\alpha$ is near zero, we observe the cross-shore evolution of bore fronts to vary
375 substantially (Fig. 12). The upstream stratification, which is strongly influenced by the
376 preceding bore, appears to be the main control on whether the bore front rarefies or steepens
377 during the transit onshore. Thus, the pre-arrival $\alpha$ is on increased importance. We observe bores

(such as that observed at OC17N 10/24 13:25) that encounter positive $\alpha$ conditions offshore and negative conditions inshore, thus becoming more rarefied during the transit to shore. We also see examples of $\alpha$ being positive at OC50, near-zero or negative at OC32N and OC25NA, and then positive at OC17N. In these instances (such as the bore observed at OC50 10/23 at 18:00), the bore will steepen, rarefy, and then steepen again.

These observations suggest that the subtidal modulation of $\alpha$ may affect how an internal bore evolves during shoaling, but a bore's influence on the waveguide and thus the evolution of the following bore will not be captured by the subtidal waveguide. Within the 2-day windows discussed (Fig. 5, 11, 12), the values of $\alpha$ estimated from sorted density are fairly constant but the bores do not all evolve similarly. This demonstrates that high-frequency changes in the waveguide, including stratification changes due the bores themselves (Fig. 8), in fact contribute to bore-to-bore variability in shoaling evolution.

2) Speed

Linear phase speeds at the northern cross shore mooring line are subtidally modulated and $c_o$ generally decreases from offshore to inshore (Figure 9d). We compare observed bore speeds to estimates of $c_o$ from the sorted and pre-arrival densities (Fig 13). Since triangle A spans the OC50 and OC40N/S moorings, one would expect the observed speeds to fall within the range of the predictions if the waves were linear. The data suggest, however, that the internal bores at this location are generally slower than $c_o$ with the exception of a few cases in October.

Speeds calculated from the sorted pre-arrival densities capture subtidal changes in bore speed, but fail to predict the observed bore-to-bore variability. The speed estimates from the pre-arrival density do predict some bore-to-bore fluctuations, but they are much smaller than and not

well-correlated with observed speeds. For example, we observe that the speed of subsequent bores can vary by 0.05-0.1m/s, but the estimates from pre-arrival density vary roughly from 0.02-0.05 m/s.

Based on our error analysis (Fig. 2), observed speed fluctuations (Fig. 13) greater than 0.035m/s (black dots) and 0.07 m/s (grey dots) indicate true bore-to-bore speed variability. Thus, the observed speed fluctuations are larger than the noise, and we can resolve bore-to-bore variations in speed. These observations suggest that subtidal and high-frequency processes that modulate waveguide will influence a bore's speed.

3) Propagation Direction

Propagation direction is estimated from the triangulation method based on observed arrival times that meet the +/-15 min threshold (Fig. 13). Unlike the observations of speed, there is little bore-to-bore variability in propagation direction. Most of the internal bores propagate from the south, and we estimate about 20% of them to propagate within +/3.5° of the shore-normal direction. There appears to be subtidal modulation of the propagation angle, but we do not explore this variability further.

*e. Bores Propagating into Shallow Water*

We utilize the entire northern cross-shore mooring transect to describe the cross-shore variability in bore speeds. Comparing the observed bore speeds (Fig. 14, red dots) to the nonrotating, long-wave linear phase speeds ($c_o$, grey/black dots) and the group velocities including rotation ($c_g$, light green dots), there is a clear distinction between the observed and theoretical estimates. Both linear speed estimates predict bores to slow down as they propagate

424 into shallow water, while the data demonstrates that bores maintain a steady speed until about
425 17m isobath. This finding corroborates the survey observations discussed in Section 3.a (Fig. 3,
426 4) and suggests there is a mechanism causing a bore to sustain speed as it transits through the
427 shoaling region.

428 The observed bore speeds are always faster than the $c_g$ estimates and are slower than $c_o$
429 estimates at depths >32m but faster than $c_o$ at shallower locations. The range of observed and
430 linear speeds can be fairly large (up to 0.25 m/s in some locations) due to subtidal changes in the
431 waveguide over the observational period (Fig 9, 13). This variability, along with the scarce
432 number of bores that can be tracked to shore with quantitative certainty, makes it difficult to
433 constrain how robust this pattern of maintained bore speed is. A fully-nonlinear, non-hydrostatic
434 model that includes rotation would be the best tool to further explore why bores maintain speed
435 during shoaling and assess how common the behavior is.

436 **4. Discussion**

437 *a. Possible Explanations for Two Bores Per Semidiurnal Period*

438 Our observation of two bores arriving within a semidiurnal period (Fig. 4, 5, 6 and Table
439 1) is not a typical finding. This pattern has been observed in Georges Bank (Lamb 1994) and
440 the New Jersey shelf (Shroyer et al. 2011), but is it uncommon compared to the majority of
441 observations which show one bore each semidiurnal period (Chereskin 1983; Holloway 1987;
442 Ramp et al. 2004; Scotti et al. 2007; Alford et al. 2010). The generation mechanism of two bores
443 each semidiurnal period has not been elicited from observations, but a fully-nonlinear numerical
444 model of Georges Bank indicates that rotation plays a key role in the formation of the second
445 semidiurnal bore by increasing long-wave dispersion (Lamb 1994). In recent years, fully-
446 nonlinear numerical models have further clarified how an internal solitary wave in the presence

447 of rotation will form a secondary, nonlinear IW due to a "decay-rebirth" cycle (Helfrich 2007;
448 Stastna et al. 2009; Grimshaw et al. 2014; Ostrovsky and Helfrich 2019). While rotation itself
449 can facilitate the formation of secondary waves, Grimshaw et al. (2014) additionally showed that
450 a shoaling wave without rotation can induce the formation of a second IW but that rotation is
451 necessary to steepen the secondary wave into a bore. It is likely that the combined effects of
452 rotation and shoaling are responsible for the two semidiurnal bores we observe, but we cannot
453 confirm the role of rotation from our observational analysis.

454 Data from this region collected in 2015 suggested the presence of only one bore per
455 semidiurnal period (Colosi et al. 2018), so this 2017 data potentially indicates interannual
456 variability of the IW field. Observations from the Oregon shelf have demonstrated the difficulty
457 in discerning the causes of IW interannual variability (Suanda and Barth 2015), and such
458 analysis is beyond the focus of this paper. However, a comparison of the 2015 and 2017
459 waveguide conditions could be a next step to addressing possible causes of IW variability.

460 This analysis also raises questions about where the bores originate. Observations of
461 propagation direction suggest the two bores come from a similar location and that the subtidal
462 shelf stratification/circulation may steer propagation (Fig. 13). We are unable to elucidate the
463 bores' generation site from this data, but we speculate that they originate either from separate
464 generation sites offset by a fixed distance or from a single generation site with complex
465 bathymetry. We could not distinguish the two bores by their characteristics – such as shape,
466 speed, or energetics – so these details were not helpful in speculating about their origin. Possible
467 generating mechanisms could be further explored with modeling tools.
468

*b. The Influence of Stratification Variability on Bore Evolution*

For a more intuitive discussion of the physical implications of $\alpha$ variability, we describe the case of a 2 layer system with no background shear:

$$\alpha = \frac{3}{2} c \frac{h_1 - h_2}{h_1 h_2} \tag{6}$$

where $h_1$ and $h_2$ are the thicknesses of the upper and lower layers respectively (Grimshaw et al. 1997). Here, the critical depth occurs when $h_1 = h_2$ and thus $\alpha = 0$. Offshore where $h_1 < h_2$, $\alpha$ is positive; but $\alpha$ becomes negative onshore of the critical depth when $h_1 > h_2$. The exact location of the critical depth varies for each IW due to changes in background stratification, but our analysis indicates that it is located between the 32m and 17m isobaths in our study region - where we frequently observe changes in steepness of the bores' leading edge.

As a bore approaches and passes through the critical depth, it's leading edge may either rarefy or steepen depending on its amplitude and the upstream conditions (Scotti et al. 2008). Thinking about the 2-layer system (Scotti et al. 2008; Baines 1998), the speed along characteristics can be described as:

$$c = \sqrt{g' \left( \frac{h_1 h_2}{h_1 + h_2} \right)} \tag{7}$$

In this framework, it is evident that the speed is maximal when $h_1 = h_2$. If $h_1 < h_2$ and $\alpha$ is positive, the top of the wave is slower-moving than the bottom and the front will steepen. If $h_1 > h_2$ and $\alpha$ is negative, the top of the wave moves faster than the bottom and the front consequently rarefies, resulting in a less-steep bore. Consistent with this theoretical framework, we observe that the bore fronts remain sharp when $\alpha$ is positive across the entire shoaling region (Fig 5). When the upstream $\alpha$ is negative, the bore fronts continue to rarefy (Fig 11). We observe several

490 instances of a bore transitioning from a sharp front to a more rarefied front when $\alpha$ is positive
491 off-shore and negative inshore (Fig 12). There are also cases where $\alpha$ fluctuates from positive to
492 negative to positive, causing the bore front to rarefy and then resteepen (Fig 12).
493 Our analysis connects the cross-shore evolution of internal bores to waveguide
494 variability. While the waveguide is modulated by subtidal processes, such as wind-driven
495 mixing and relaxations of the coastal current (Fig. 7, 9), there is also high-frequency variability
496 driven by the bores themselves (Fig. 5, 8). We demonstrate that these subtidal and high-
497 frequency changes in stratification (Fig. 8) both influence a bore's cross-shore evolution (Fig. 5)
498 and speed (Fig. 13). For example, even during periods when the subtidal waveguide is fairly
499 constant (Fig. 9), subsequent bores do not evolve consistently (Fig 5, 11, 12) or propagate at the
500 same speed (Fig. 13). We conclude that especially in a region with two semidiurnal bores, bore-
501 to-bore variability in shoaling evolution is likely driven by a confluence of factors, including a
502 bore's impact on the waveguide of the next bore and stratification variability due to the wind
503 (Fig. 10).
504 Our findings corroborate Holloway et al.'s (1997) conclusion that $\alpha$'s high-frequency
505 variability plays a key role in determining a bore's transformation during shoaling. Comparing
506 the temporal variability of $\alpha$ across the shoaling region, we note that values are correlated at
507 50/40m and 25/17m (Fig. 9). While $\alpha$ at the 100 isobath is subtidally modulated but always
508 positive, $\alpha$ at 50/40m is subtidally modulated and fluctuates between positive and negative
509 values. At the 25/17m and 10m isobaths, $\alpha$ has higher-frequency and larger-magnitude
510 fluctuations. Synthesizing this information with the off-shore subtidal wind correlations (Fig 10,
511 Table 4), the effect of stratification on $\alpha$ (Fig 8), and a bore's influence on the stratification
512 ahead of the subsequent bore (Fig 5, 11, 12), we conclude that the cross-shore gradient in $\alpha$ can

513 evolve substantially in the timeframe a bore is propagating onshore. This will affect how a
514 bore's leading edge will evolve across the inner shelf.
515 While the 100m mooring has a muted response to wind relaxations, the locations <25m
516 experience quick (<1 day) changes in stratification and $\alpha$ after a relaxation event. The impact of
517 offshore, subtidal winds on nearshore stratification in this region has been shown to have
518 important along- and cross-shore variability (Aristizábal et al. 2017; Melton et al. 2009), but it's
519 impact on the waveguide is an open research topic. Our observations suggest that regional,
520 subtidal winds contribute to modulation of the cross-shore waveguide, but it is unclear what the
521 spatial footprint of this is or if local winds are comparably important.
522 Temporal waveguide changes and internal bore evolution over our observational period
523 appear to be disconnected from variability in the semidiurnal kinetic energy density. For
524 example, $\alpha$ and $c_o$ appear to have lower-frequency modulation than the depth-averaged
525 semidiurnal kinetic energy. Comparing the September and October data, we do not observe any
526 changes in the IW field but there is significant shift in the cross-shore kinetic energy gradient. In
527 October, there is more kinetic energy at MS100 and less at OC25NA, meaning that in the latter
528 half of the record there is a larger kinetic energy loss across the shoaling region. We presume
529 that this kinetic energy loss could be associated with stronger dissipation or IW breaking, but are
530 unable to confirm this.
531
532 *c. Observations vs Theory*
533 The observed bore speeds are always faster than $c_g$ estimates and are generally slower
534 than $c_o$ offshore of the 32m isobath and faster than $c_o$ farther inshore (Fig. 14). Several studies
535 have suggested that rotation must be accounted for when calculating the speed of an internal bore

536 (Grimshaw et al. 1998; Grimshaw and Helfrich 2012; Colosi et al. 2018) and that the group
537 velocity is the appropriate calculation (equation 5). However, given the timescales associated
538 with sharp bore fronts (a few mins – 1.5 hours) and the presence an $M_2$ bore every 6 hours, it is
539 not obvious that a semidiurnal frequency is appropriate to use in calculating $c_g$. Consistent with
540 findings by Lamb (1994), we demonstrate that at the semidiurnal frequency, $c_g$ estimates are
541 slower than $c_o$ by 0.04-0.10 $ms^{-1}$. The nonrotating long-wave phase speed $c_o$, has been used for
542 comparison against observations in similar analyses (Lamb 1994; Grimshaw et al. 2004; Shroyer
543 et al. 2011; Thomas et al. 2016) and has a comparable cross-shore pattern to $c_g$. The impacts of
544 rotation on bore speeds remains an open research question, which we cannot thoroughly address
545 in this analysis.

546 Both linear speed estimates predict that the bores slow down as they transit into shallower
547 water, but observations indicate the bores maintain a steady speed over most of the shoaling
548 region (Figs. 3, 4, 14) and begin to decelerate between the 17m and 10m isobaths. We cannot
549 elucidate from this dataset the reason that the bores maintain their speed during shoaling and
550 suggest that a fully-nonlinear model with rotation would be best to further explore the
551 mechanisms that control a shoaling bore's speed.

552 Subtidal changes in stratification appear to modulate bore speeds, but there is additional
553 bore-to-bore speed variability whose magnitude and timing are not explained by the upstream
554 stratification (Fig 13). One possible explanation is that neither the pre-arrival nor sorted
555 densities are representative of the waveguide in a region dominated by 2 semidiurnal internal
556 tides. Comparing our data to observations from regions with only one observed bore per
557 semidiurnal period (Holloway et al. 1997; Scotti et al. 2008; Thomas et al. 2016), it appears that
558 bore-to-bore interactions may facilitate more nonlinear feedbacks when the pycnocline has not

559 yet relaxed to its background position before the arrival of the next bore. The shape/evolution of
560 the internal bores we observe are similar to published observations, but the previous internal bore
561 appears to be a stronger influence here. This is also consistent with numerical work by Lamb
562 and Warn-Varnas (2015), which demonstrated that an IW may influence the upstream conditions
563 ahead of a subsequent wave and that the *local* upstream profile of the second wave (i.e., the
564 profile trailing the first wave) is a good indicator of the second wave's amplitude/shape.
565 Our exclusion of background current in calculations of $c_o$ and $\alpha$ allows us to better
566 understand how stratification influences the shoaling bores, but there are consequently open
567 questions related to the importance of local shear that should be addressed in further work. One
568 motivating factor to exclude shear was the sensitivity of the wave properties to how the
569 "background shear" was defined and the uncertainty, especially given the presence of bores
570 every ~6 hrs, regarding the appropriate definition. Local upstream conditions can look quite
571 different from a time-averaged or low-passed profile (Lamb and Warn-Varnas 2015), and the
572 vertical structure of the horizontal shear profile determines how strongly wave properties are
573 influenced by the background current (Stastna and Lamb 2002). Thus, it is possible that bore-to-
574 bore changes in the shear contribute to the unexplained linear bore speed variability.
575

576 **5. Conclusion**

577 We observe two tidal bores arrive every semidiurnal period, 72% of which can be tracked
578 from the 100m isobath to the 10m isobath. These large amplitude bores propagate from roughly
579 the same direction and are offset by ~ 6 hours. The bore speeds are subtidally modulated, but
580 there is additional bore-to-bore speed variability (as large as 10 cm/s) that is not explained by the
581 stratification immediately upstream of the bores. It remains an open question what dynamics

582 drive these observed bore-to-bore speed fluctuations. Measured bore speeds are always faster
583 than the linear rotating group velocities and are generally slower than the linear longwave
584 nonrotating phase speeds ($c_o$) offshore of the 32m isobath and faster than $c_o$ further inshore.
585 Contrary to both linear speed estimates which predict bores to slow while transiting into
586 shallower depths, the bores maintain a steady speed over most of the shoaling region and start to
587 slow only between 17m and 10m.

588 The waveguide, including stratification and $c_o$, varies across the shoaling region and
589 evolves over the observational period. We use $\alpha$ as a metric to describe stratification, and
590 generally $\alpha$ is always positive offshore (~100m) and more variable inshore. We observe that the
591 critical depth, where $\alpha$ changes sign, is located between the 32m and 17m isobaths for the
592 majority of the bores. Lagged correlation analyses between subtidal $\alpha$ at each mooring and the
593 subtidal, offshore winds reveal that stratification in the shallower region (< 25m) is impacted by
594 wind changes while the deeper region (> 40m) has a muted response. In addition to modulation
595 of the waveguide by subtidal processes, such as wind-driven mixing, upwelling and
596 downwelling, and relaxations of the coastal current, there is also higher-frequency variability of
597 the waveguide driven by the bores themselves. Each bore modifies the conditions the subsequent
598 bore propagates through and, given that the bore itself evolves during shoaling, this can
599 contribute to strong cross-shore gradients in the waveguide on short timescales (< 6hrs). Since
600 there are two bores per semidiurnal period in this region, the influence of the bores on the
601 waveguide is especially important compared to other regions where only one bore per
602 semidiurnal period has been observed.

603 The steepness of a bore's leading edge depends on the upstream waveguide, and we
604 demonstrated that the cross-shore evolution of a bore is determined by the cross-shore gradient

of $\alpha$. The bore fronts are steep when $\alpha$ ahead of the bore is positive and are more rarefied when the upstream $\alpha$ is near zero or negative. In the case of $\alpha$ being positive offshore and negative inshore, we observe the bores leading edge to decrease in steepness while shoaling. However, due to the high-frequency fluctuations in $\alpha$ caused by the bores themselves, there are also instances where $\alpha$ is negative/near zero offshore compared to inshore. In these cases, the rarefied leading edge of the wave resteepens into a sharp bore. Because high-frequency changes in the waveguide are so important in this region, there can be significant bore-to-bore variability in the cross-shore evolution of the bores during similar subtidal waveguide conditions.

Our observations demonstrated that the coastal waveguide has complex spatiotemporal variability modulating the evolution of shoaling internal bores. These findings suggest that mixing on the inner shelf, which depends on how/when/where internal waves break, will also be influenced by variability of cross-shore gradients in the waveguide.

**Acknowledgements**

We thank the personnel who helped on the R/V Oceanus and R/V Sally Ride during mooring operations and surveying. Funding was provided by the Office of Naval Research Inner Shelf Departmental Research Initiative. Data on the project-scale is in the process of being archived, but data presented in this paper can be immediately accessed by emailing Dr. Jacqueline McSweeney at jmcsweeney@coas.oregonstate.edu.

**References**


Alford, M. H., R.-C. Lien, H. Simmons, J. Klymak, S. Ramp, Y. J. Yang, D. Tang, and M.-H. Chang, 2010: Speed and Evolution of Nonlinear Internal Waves Transiting the South China Sea. *J. Phys. Oceanogr.*, doi:10.1175/2010JPO4388.1.

Apel, J. R., 2003: A new analytical model for internal solitons in the ocean. *J. Phys. Oceanogr.*, **33**, 2247–2269.

Aristizábal, M. F., M. R. Fewings, and L. Washburn, 2017: Effects of the Relaxation of Upwelling-Favorable Winds on the Diurnal and Semidiurnal Water Temperature Fluctuations in the Santa Barbara Channel, California. *J. Geophys. Res. Ocean.*, **122**, 7958–7977.

Baines, P. G., 1998: *Topographic effects in stratified flows*. Cambridge university press,.

Cairns, J. L., 1967: Asymmetry of internal tidal waves in shallow coastal waters. *J. Geophys. Res.*, **72**, 3563–3565.

Chereskin, T. K., 1983: Generation of internal waves in Massachusetts Bay. *J. Geophys. Res.*, doi:10.1029/JC088iC04p02649.

Colosi, J. A., N. Kumar, S. H. Suanda, T. M. Freismuth, and J. H. MacMahan, 2018: Statistics of Internal Tide Bores and Internal Solitary Waves Observed on the Inner Continental Shelf off Point Sal, California. *J. Phys. Oceanogr.*, doi:10.1175/JPO-D-17-0045.1.

Grimshaw, R., and K. Helfrich, 2012: The effect of rotation on internal solitary waves. *IMA J. Appl. Math.*, **77**, 326–339.

——, E. Pelinovsky, and T. Talipova, 1997: The modified Korteweg-de Vries equation in the theory of large-amplitude internal waves. *Nonlinear Process. Geophys.*, doi:10.5194/npg-4-237-1997.

——, E. Pelinovsky, and O. Poloukhina, 2002: Higher-order Korteweg-de Vries models for internal solitary waves in a stratified shear flow with a free surface. *Nonlinear Process. Geophys.*, **9**, 221–235.

——, ——, T. Talipova, and A. Kurkin, 2004: Simulation of the Transformation of Internal Solitary Waves on Oceanic Shelves. *J. Phys. Oceanogr.*, doi:10.1175/JPO2652.1.

——, C. Guo, K. Helfrich, and V. Vlasenko, 2014: Combined effect of rotation and topography on shoaling oceanic internal solitary waves. *J. Phys. Oceanogr.*, **44**, 1116–1132.

Grimshaw, R. H. J., L. A. Ostrovsky, V. I. Shrira, and Y. A. Stepanyants, 1998: Long nonlinear surface and internal gravity waves in a rotating ocean. *Surv. Geophys.*, **19**, 289–338.

Helfrich, K. R., 2007: Decay and return of internal solitary waves with rotation. *Phys. fluids*, **19**, 26601.

Helfrich, K. R., W. K. Melville, and J. Miles, 1984: On interfacial solitary waves over slowly varying topography. *J. Fluid Mech.*, doi:10.1017/S0022112085001938.

Henyey, F. S., and A. Hoering, 1997: Energetics of borelike internal waves. *J. Geophys. Res. Ocean.*, **102**, 3323–3330.

Holloway, P. E., 1987: Internal hydraulic jumps and solitons at a shelf break region on the Australian North West Shelf. *J. Geophys. Res. Ocean.*, **92**, 5405–5416.

——, E. Pelinovsky, T. Talipova, and B. Barnes, 1997: A nonlinear model of internal tide transformation on the Australian North West Shelf. *J. Phys. Oceanogr.*, **27**, 871–896.

Lamb, K. G., 1994: Numerical experiments of internal wave generation by strong tidal flow across a finite amplitude bank edge. *J. Geophys. Res. Ocean.*, **99**, 843–864.

——, 2002: A numerical investigation of solitary internal waves with trapped cores formed via shoaling. *J. Fluid Mech.*, **451**, 109–144.

——, and L. Yan, 1996: The evolution of internal wave undular bores: comparisons of a fully nonlinear numerical model with weakly nonlinear theory. *J. Phys. Oceanogr.*, **26**, 2712–2734.

Lamb, K. G., and A. Warn-Varnas, 2015: Two-dimensional numerical simulations of shoaling internal solitary waves at the ASIAEX site in the South China Sea. *Nonlinear Process. Geophys.*, **22**, 289–312.

Lee, C., and R. C. Beardsley, 1974: The generation of long nonlinear internal waves in a weakly stratified shear flow. *J. Geophys. Res.*, **79**, 453–462.

Lee, O. S., 1961: Observations on internal waves in shallow water. *Limnol. Oceanogr.*, **6**, 312–321.

Lerczak, J. A., C. D. Winant, and M. C. Hendershott, 2003: Observations of the semidiurnal internal tide on the southern California slope and shelf. *J. Geophys. Res.*, doi:10.1029/2001JC001128.

——, and Coauthors, 2019: Untangling a web of interactions where surf meets coastal ocean. *Eos (Washington. DC).*, **100**, doi:10.1029/2019EO122141.

Li, Q., and D. M. Farmer, 2011: The Generation and Evolution of Nonlinear Internal Waves in the Deep Basin of the South China Sea. *J. Phys. Oceanogr.*, doi:10.1175/2011JPO4587.1.

Melton, C., L. Washburn, and C. Gotschalk, 2009: Wind relaxations and poleward flow events in a coastal upwelling system on the central California coast. *J. Geophys. Res. Ocean.*, **114**.

Moum, J. N., D. M. Farmer, W. D. Smyth, L. Armi, and S. Vagle, 2003: Structure and generation of turbulence at interfaces strained by internal solitary waves propagating shoreward over the continental shelf. *J. Phys. Oceanogr.*, **33**, 2093–2112.

Ostrovsky, L. A., and K. R. Helfrich, 2019: Some New Aspects of the Joint Effect of Rotation

and Topography on Internal Solitary Waves. *J. Phys. Oceanogr.*, **49**, 1639–1649.

Perry, R. B., and G. R. Schimke, 1965: Large-amplitude internal waves observed off the Northwest Coast of Sumatra. *J. Geophys. Res.*, doi:10.1029/JZ070i010p02319.

Pineda, J., 1991: Predictable upwelling and the shoreward transport of planktonic larvae by internal tidal bores. *Science (80-. ).*, **253**, 548–549.

Pineda, J., 1999: Circulation and larval distribution in internal tidal bore warm fronts. *Limnol. Oceanogr.*, **44**, 1400–1414.

Ramp, S. R., and Coauthors, 2004: Internal solitons in the northeastern South China Sea. Part I: Sources and deep water propagation. *IEEE J. Ocean. Eng.*, **29**, 1157–1181.

Scotti, A., and J. Pineda, 2004: Observation of very large and steep internal waves of elevation near the Massachusetts coast. *Geophys. Res. Lett.*, **31**.

Scotti, A., B. Butman, R. C. Beardsley, P. S. Alexander, and S. Anderson, 2005: A modified beam-to-earth transformation to measure short-wavelength internal waves with an acoustic Doppler current profiler. *J. Atmos. Ocean. Technol.*, doi:10.1175/JTECH1731.1.

Scotti, A., R. C. Beardsley, and B. Butman, 2007: Generation and propagation of nonlinear internal waves in Massachusetts Bay. *J. Geophys. Res. Ocean.*, **112**.

Scotti, A., R. C. Beardsley, B. Butman, and J. Pineda, 2008: Shoaling of nonlinear internal waves in Massachusetts Bay. *J. Geophys. Res. Ocean.*, doi:10.1029/2008JC004726.

Shroyer, E. L., J. N. Moum, and J. D. Nash, 2009: Observations of Polarity Reversal in Shoaling Nonlinear Internal Waves. *J. Phys. Oceanogr.*, doi:10.1175/2008JPO3953.1.

——, ——, and ——, 2010: Energy transformations and dissipation of nonlinear internal waves over New Jersey's continental shelf. *Nonlinear Process. Geophys.*, doi:10.5194/npg-17-345-2010.

Shroyer, E. L., J. N. Moum, and J. D. Nash, 2011: Nonlinear internal waves over New Jersey's continental shelf. *J. Geophys. Res. Ocean.*, **116**.

Stanton, T. P., and L. A. Ostrovsky, 1998: Observations of highly nonlinear internal solitons over the continental shelf. *Geophys. Res. Lett.*, doi:10.1029/98GL01772.

Stastna, M., and K. G. Lamb, 2002: Large fully nonlinear internal solitary waves: The effect of background current. *Phys. fluids*, **14**, 2987–2999.

Stastna, M., F. J. Poulin, K. L. Rowe, and C. Subich, 2009: On fully nonlinear, vertically trapped wave packets in a stratified fluid on the f-plane. *Phys. Fluids*, **21**, 106604.

Suanda, S. H., and J. A. Barth, 2015: Semidiurnal baroclinic tides on the central Oregon inner shelf. *J. Phys. Oceanogr.*, **45**, 2640–2659.

Thomas, J. A., J. A. Lerczak, and J. N. Moum, 2016: Horizontal variability of high-frequency nonlinear internal waves in Massachusetts Bay detected by an array of seafloor pressure sensors. *J. Geophys. Res. Ocean.*, **121**, 5587–5607, doi:10.1002/2016JC011866. http://doi.wiley.com/10.1002/2016JC011866 (Accessed January 9, 2018).

Vlasenko, V., and K. Hutter, 2002: Numerical experiments on the breaking of solitary internal wavesover a slope–shelf topography. *J. Phys. Oceanogr.*, **32**, 1779–1793.

Vlasenko, V., and N. Stashchuk, 2007: Three-dimensional shoaling of large-amplitude internal waves. *J. Geophys. Res. Ocean.*, **112**.

Walter, R. K., C. Brock Woodson, R. S. Arthur, O. B. Fringer, and S. G. Monismith, 2012: Nearshore internal bores and turbulent mixing in southern Monterey Bay. *J. Geophys. Res. Ocean.*, doi:10.1029/2012JC008115.

Winters, K. B., P. N. Lombard, J. J. Riley, and E. A. D'Asaro, 1995: Available potential energy and mixing in density-stratified fluids. *J. Fluid Mech.*, doi:10.1017/S002211209500125X.

**Tables**

| Mooring | # of bores identified | Identified bores/ Observational days | Mean # of hours between subsequent bores | STD of Mean # of Hours between subsequent bores | # of tracked bores | Tracked bores with +/- 15 min cutoff flag | Tracked bores with +/- 7.5 min cutoff flag |
|---|---|---|---|---|---|---|---|
| MS100 | 178 | 3.34 | 7.08 | 3.21 | 148 | 102 | 67 |
| OC50 | 158 | 3.11 | 7.90 | 3.59 | 148 | 105 | 82 |
| OC40N | 141 | 2.68 | 8.39 | 4.56 | 139 | 79 | 64 |
| OC40S | 149 | 2.91 | 7.93 | 3.60 | 139 | 93 | 67 |
| OC32N | 142 | 2.55 | 8.75 | 3.90 | 138 | 65 | 46 |
| OC32S | 146 | 2.70 | 8.65 | 4.24 | 132 | 79 | 56 |
| OC25NA | 132 | 2.39 | 9.03 | 4.14 | 131 | 69 | 38 |
| OC25NB | 133 | 2.56 | 8.97 | 4.02 | 131 | 63 | 46 |
| OC25M | 130 | 2.50 | 8.98 | 3.95 | 130 | 70 | 49 |
| OC25SB | 126 | 2.47 | 9.05 | 4.16 | 126 | 64 | 50 |
| OC25SA | 129 | 2.49 | 8.47 | 3.85 | 129 | 73 | 55 |
| OC17N | 118 | 2.14 | 9.56 | 4.27 | 116 | 60 | 45 |
| OC17S | 113 | 2.05 | 9.58 | 4.31 | 111 | 61 | 42 |
| OC10N | 64 | 2.07 | 9.89 | 5.70 | 64 | 31 | 19 |
| STR3B-9 | 69 | 1.58 | 9.81 | 5.36 | 69 | 33 | 17 |

Table 1. Information about the internal bores tracked through the Oceano mooring array. For the number of hours between subsequent bores, this includes all times (even though Fig. 6 includes only cases <24hrs)

| Triangle | # estimates 7.5/15 | Mean Speed (cm/s) | Standard deviation (cm/s) | Mean angle (degrees, 0° is east) | Standard deviation of angle (degrees) |
|---|---|---|---|---|---|
| A | 32 / 53 | 20.6 / 21.1 | 4.6 / 5.2 | 5.1/ 6.4 | 11.9 / 13.0 |
| B | 39 / 65 | 18.3 / 18.4 | 4.0 / 4.1 | 4.3/ 5.2 | 13.2 / 13.6 |
| C | 37 / 66 | 16.5 / 16.6 | 4.8 / 5.8 | 2.5/ 1.2 | 10.0 / 12.4 |
| D | 33 / 48 | 16.6 / 16.2 | 6.2 / 5.8 | 1.8 / 0.4 | 10.9 / 12.0 |
| E | 15 / 30 | 14.4 / 13.1 | 4.1 / 4.7 | -4.4 / -5.8 | 10.0 / 9.5 |

Table 2. The number of estimates of speed/direction from bore arrivals, the mean speed (cm/s), the standard deviation in speed (cm/s), the propagation angle (degrees relative to east, positive is propagating to the north), and standard deviation of the angle for triangles A-E shown in Fig 1. For all columns, the estimates correspond to bores flagged by the +/-7.5min (left) and +/-15 (right) min certainty thresholds (section 2.b.2) .

| Time (hrs) | ΔH | H | ΔH/H |
|---|---|---|---|
| 0 | 23.7 | 51.6 | 0.46 |
| 1.3 | 22.0 | 45.9 | 0.48 |
| 3.8 | 17.2 | 36.7 | 0.47 |
| 4.7 | 16.7 | 35.1 | 0.48 |
| 6.2 | 11.4 | 28.0 | 0.41 |
| 6.9 | 11.5 | 24.5 | 0.47 |

Table 3. The estimation of the bore's amplitude from Fig. 3, where ΔH is the vertical pycnocline displacement and H is the total water depth, using the 13° isotherm as proxy for the pycnocline.

| Mooring | $R^2$ between subtidal wind speed (>33hrs) and negative $\alpha$ | Lag Time (hrs) | $R^2$ for lagged correlation between subtidal wind speed (>33hrs) and negative $\alpha$ |
|---|---|---|---|
| MS100 | 0.002 | 0 | 0. 002 |
| OC50 | 0.048 | 0 | 0. 048 |
| OC40N | 0.053 | 0 | 0. 053 |
| OC25NA | 0.252 | 3 | 0.278 |
| OC17N | 0.274 | 1 | 0.282 |
| OC10N | 0.186 | 2 | 0.196 |

Table 4. Negative correlation coefficients for the subtidal wind speed and $\alpha$ at shoaling mooring locations. Lagged correlation statistics are also shown. Timeseries for statistically significant moorings are shown in Fig. 10.

**Figures**

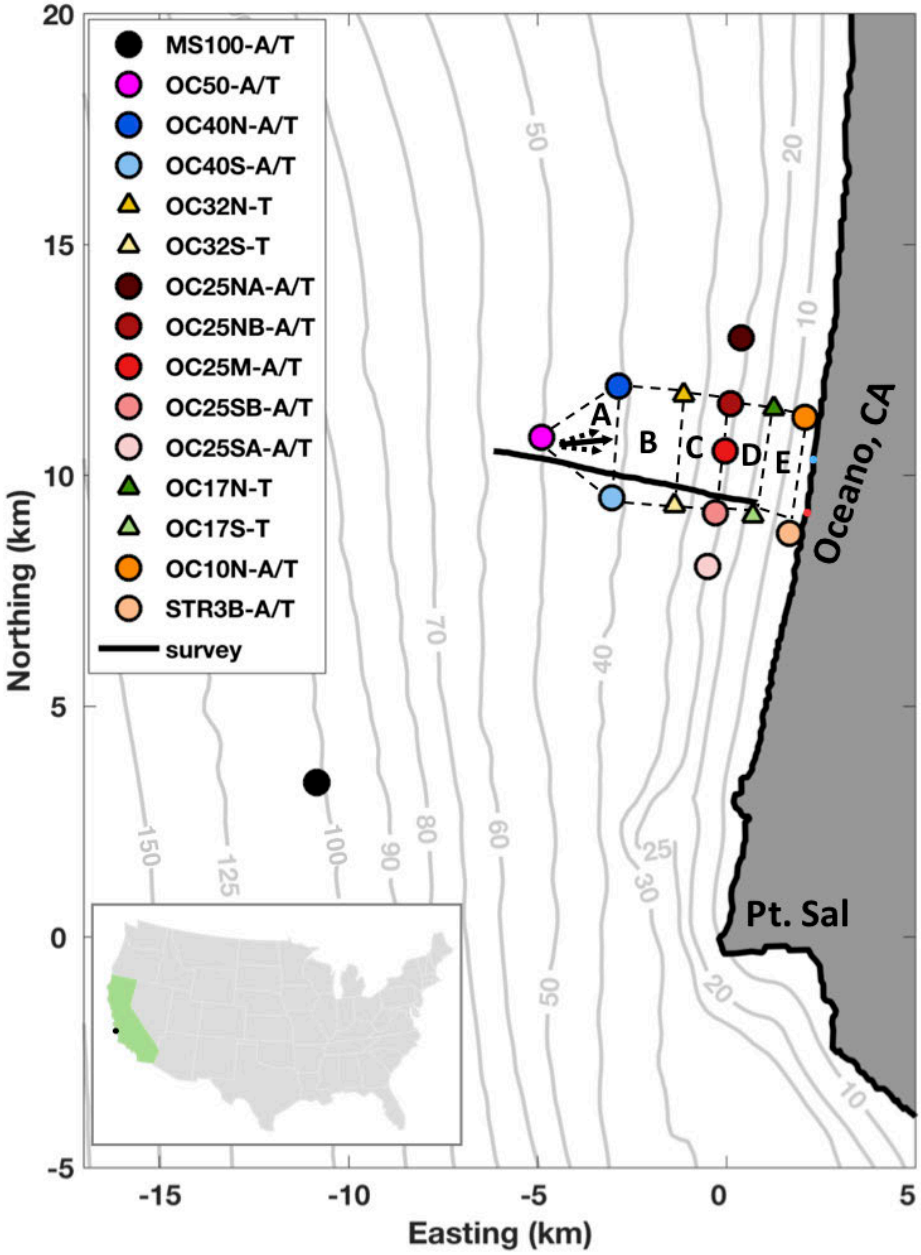


Figure 1. Map of the 15 moorings used in this analysis with bathymetry contoured in light grey. The site location is offshore of Oceano, California and the east-north coordinate system is centered on the tip of Pt. Sal. The mooring names are coded such that the first 2-3 letters indicate the broader location (MS = mid shelf, OC = Oceano inner shelf, and STR = nearshore), the following numbers indicate the water depth, and the letters at the end indicate the type of

mooring design (A= lander with upward looking ADCP, T= string mooring with temperature sensors spaced vertically every ~1-2m). For the moorings on the 25m isobath, they are labeled from north to south respectively via “NA”, “NB”, “M”, “SB”, and “SA”. Six cross-shore transects with a towed-CTD were conducted from the R/V Oceanus September 9, 2017 (thick black line). Dashed triangles and rectangles (labeled with black letters A-E) denote the groups of moorings used for the speed and angle calculations discussed in Section 2.b.3. The solid black arrow shows the mean propagation direction of bores at triangle A (Fig. 13) and the dashed arrows denote +/- 1 standard deviation (detailed in Table 2). The red/green dot on the coast denotes the coastline location for Fig. 3/14.

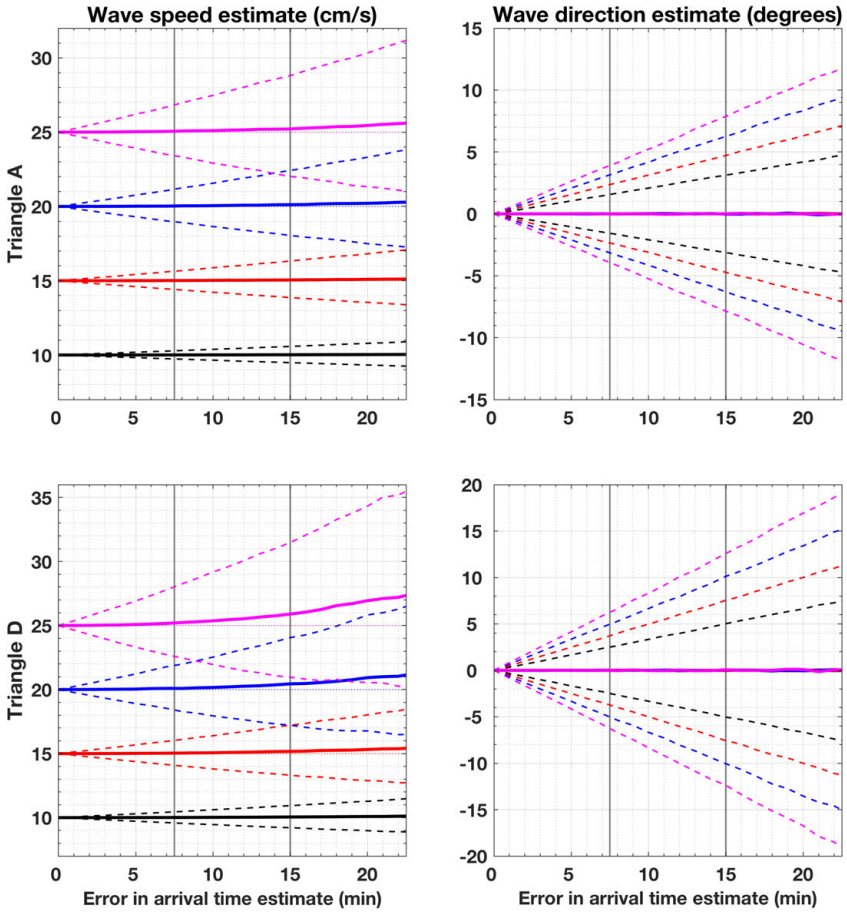


Figure 2. Left panels) Wave speed estimate (cm/s) from 10000 synthetic waves of known speeds and angle as a function of the error in arrival time (mins) for triangle A (top) and rectangle D (bottom) shown in Fig. 1. Four wave speed cases were run – 10, 15, 20, and 25 cm/s – distinguished by black, red, blue, and magenta, respectively. Solid lines show the average value, dashed lines show 95% confidence limits. The vertical lines indicates the +/-7.5 and +/15min threshold cutoffs for step 3 of bore identification (section 2.b.2). Right panels) Same setup as left panels but for wave direction estimate (degrees).

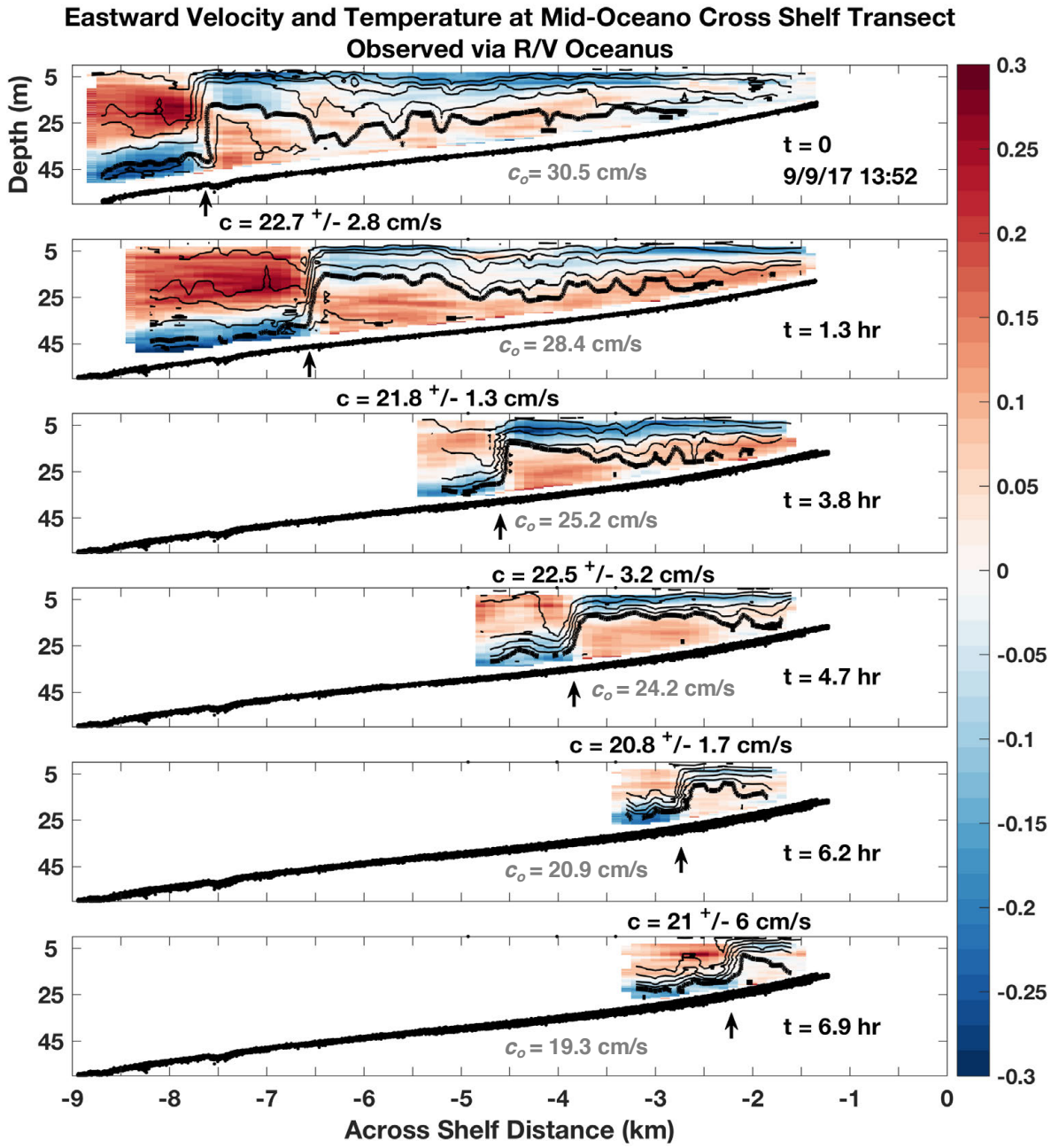


Figure 3. Eastward velocity (colored, with positive values towards east) with 1°C temperature isotherms contoured (13°C isotherm bold) from towed surveys along the course shown in Fig. 1. The thick black line denotes the bed depth from the ship's echosounder. Each panel shows a separate transect, with time progressing down the figure. The timestamp in each panel corresponds with the passage of the bore front, indicated with a black arrow, and counting from

t=0 (September 9, 2017 13:52 UTC). The across-shelf distance is measured from the nearest location to the coastline if the transect path were to continue and intersect the shore (red dot in Fig. 1). The bore speeds estimated from distance traveled between bore passages are noted between the respective panels along with error estimates. The nonrotating longwave linear phase speeds ($c_o$) estimated at the time/location of bore passage estimated from nearby moorings are shown in grey in each panel.

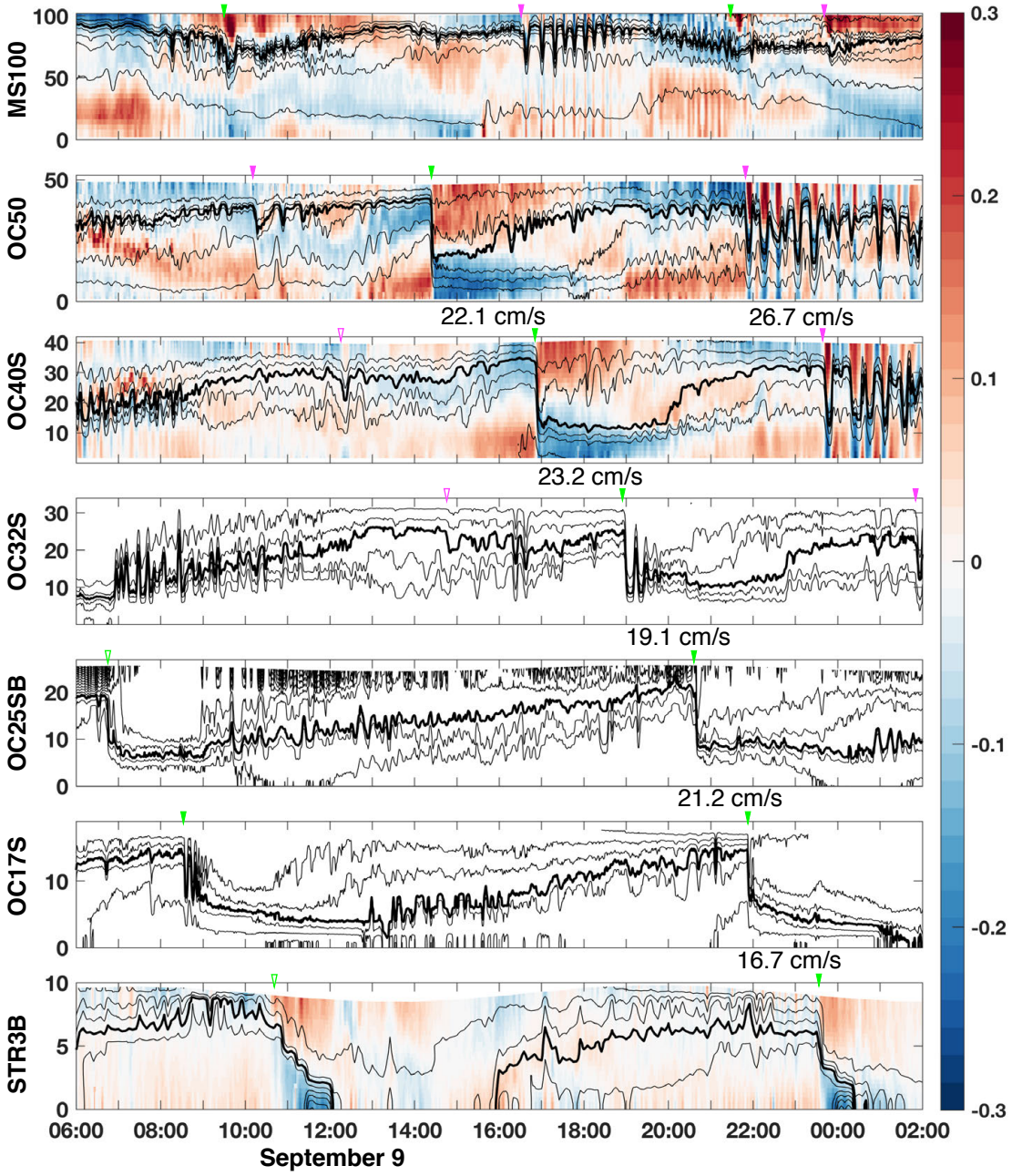


Figure 4. Eastward velocity colored (3min-16hr bandpass filtered, with positive values towards east) and temperature contoured (black lines, 1° contours with 15° isotherm bold) from MS100, OC50, OC40S, OC32S, OC25SB, OC17S, and STR3B (top to bottom panel) for September 9 06:00 to September 10 02:00 2017 (UTC). The y-axis is meters above the bed. Bore arrivals are indicated by alternating green and magenta triangles, where solid triangles show arrivals that

meet the +/- 15 min certainty threshold and the triangles with a white center don't. Available speed estimates from triangulation method (Table 2) are shown between panels.

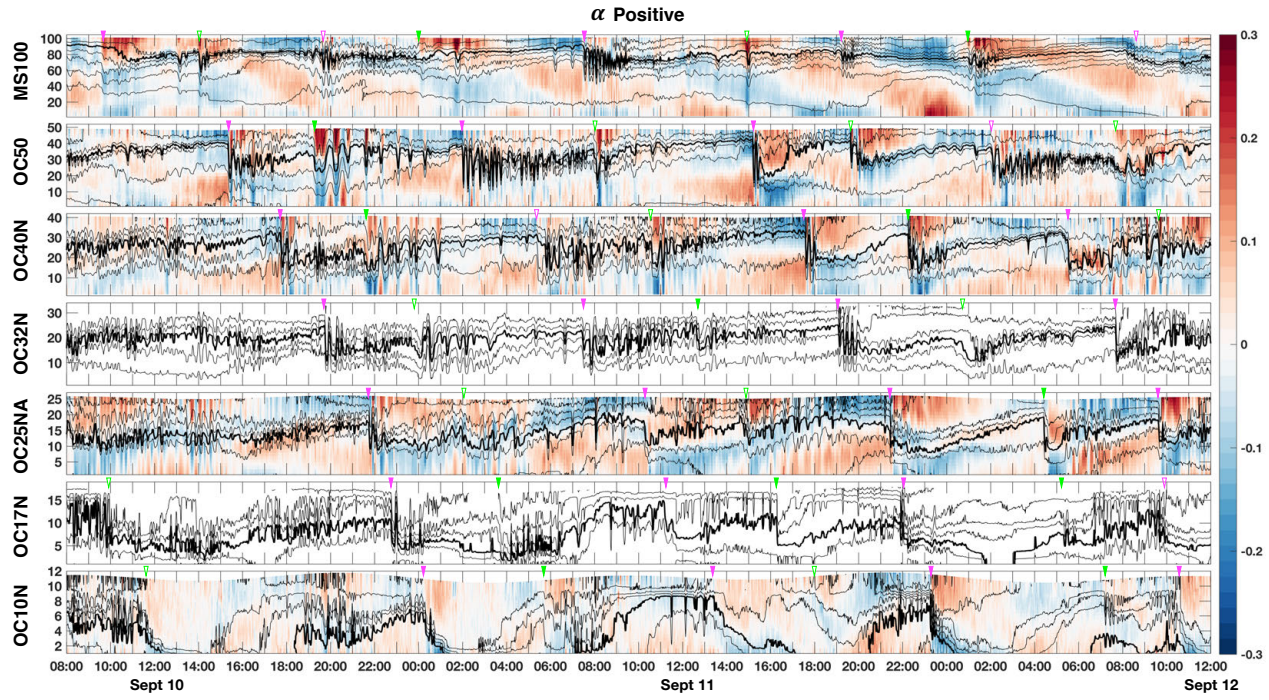


Figure 5. Same configuration as Fig. 4 except for moorings MS100, OC50, OC40N, OC32N, OC25NA, OC17N, and OC10N (top to bottom panel) for September 10 00:00 to September 12 12:00 2017 (UTC).

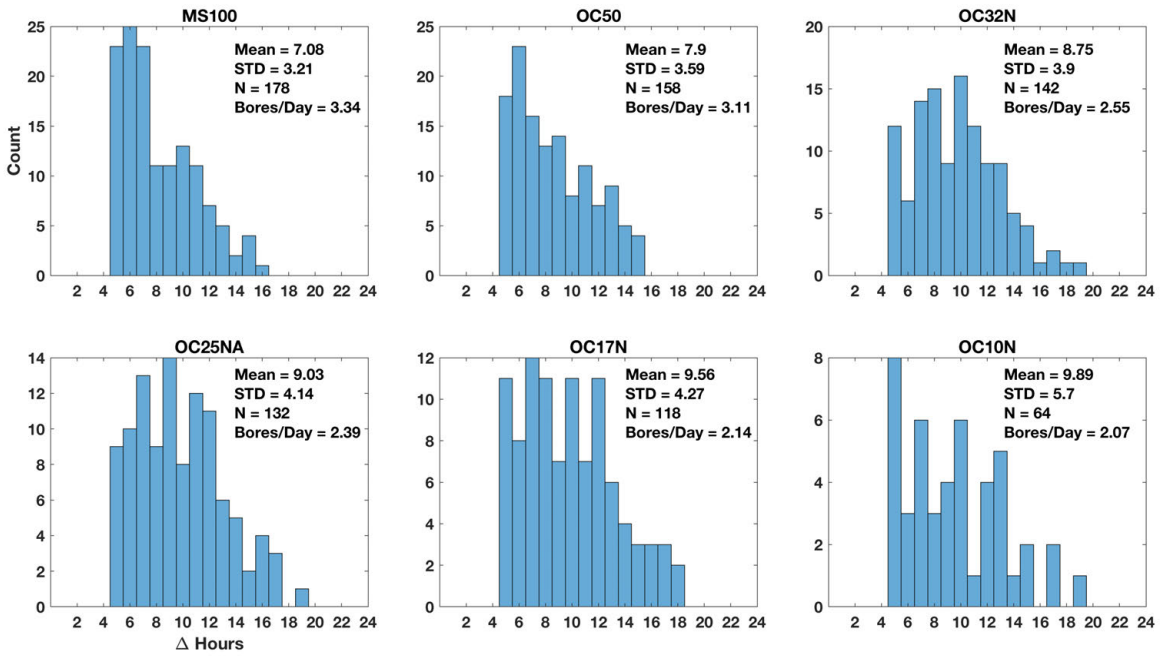


Figure 6. Histograms of the number of hours between subsequent bores at MS100, OC50, OC32N, OC25NA, OC17N, and OC10N moorings. N is the number of bores identified at that location (as discussed in section 2.b.1). We exclude when Δ hours is greater than 24 hrs for plotting (not statistics). The statistics shown here are also given in Table 1.

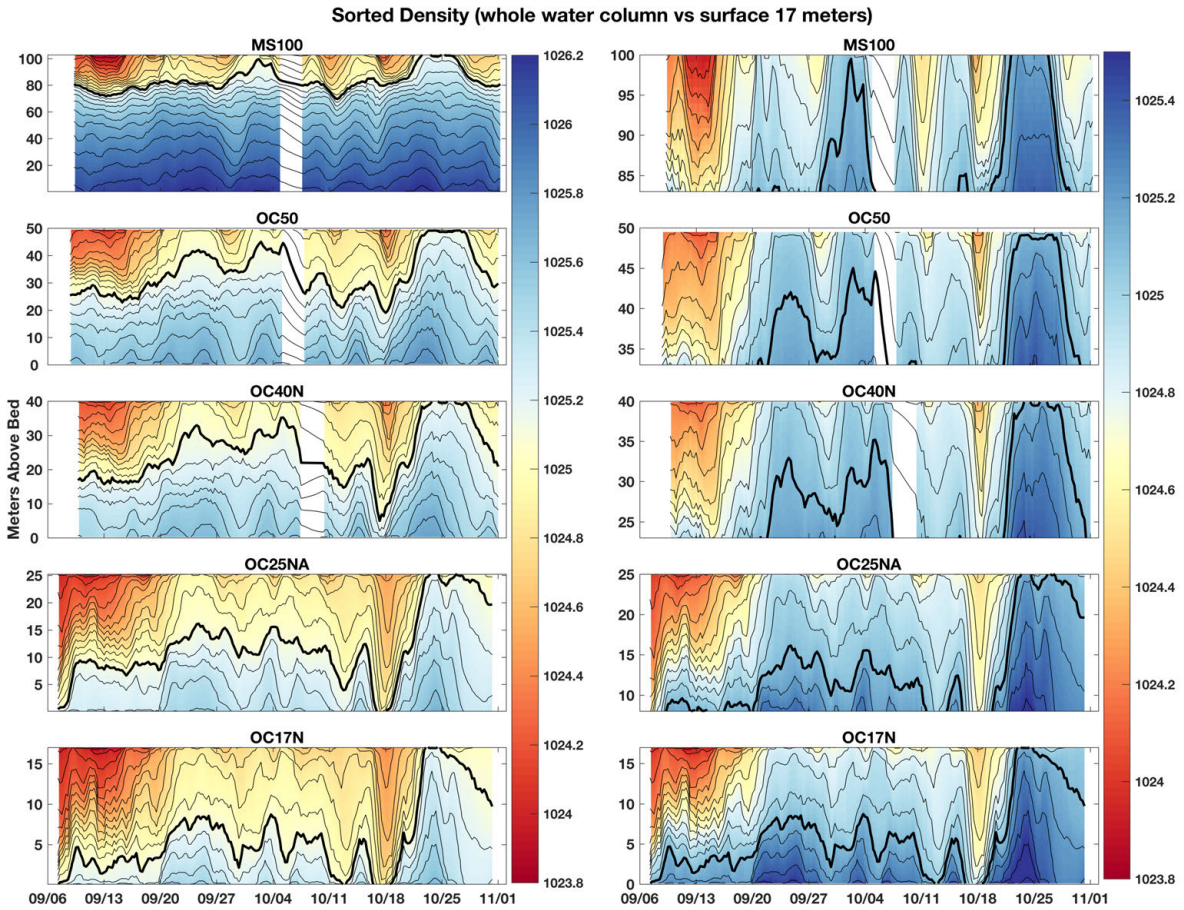


Figure 7. Sorted density (kg/m$^3$) as described in section 2.b.1 for MS100 (top panel), OC50, OC40N, OC25NA, and OC17N (bottom) moorings. Left panels show the whole water column; right panels show only the topmost 17m. The 0.1 kg/m$^3$ isopycnal intervals are contoured (black lines), and the 1025.1 kg/m$^3$ isopycnal is bold. The y-axis for all panels is meters above the bed. Temporal gaps are when moorings were out of the water.

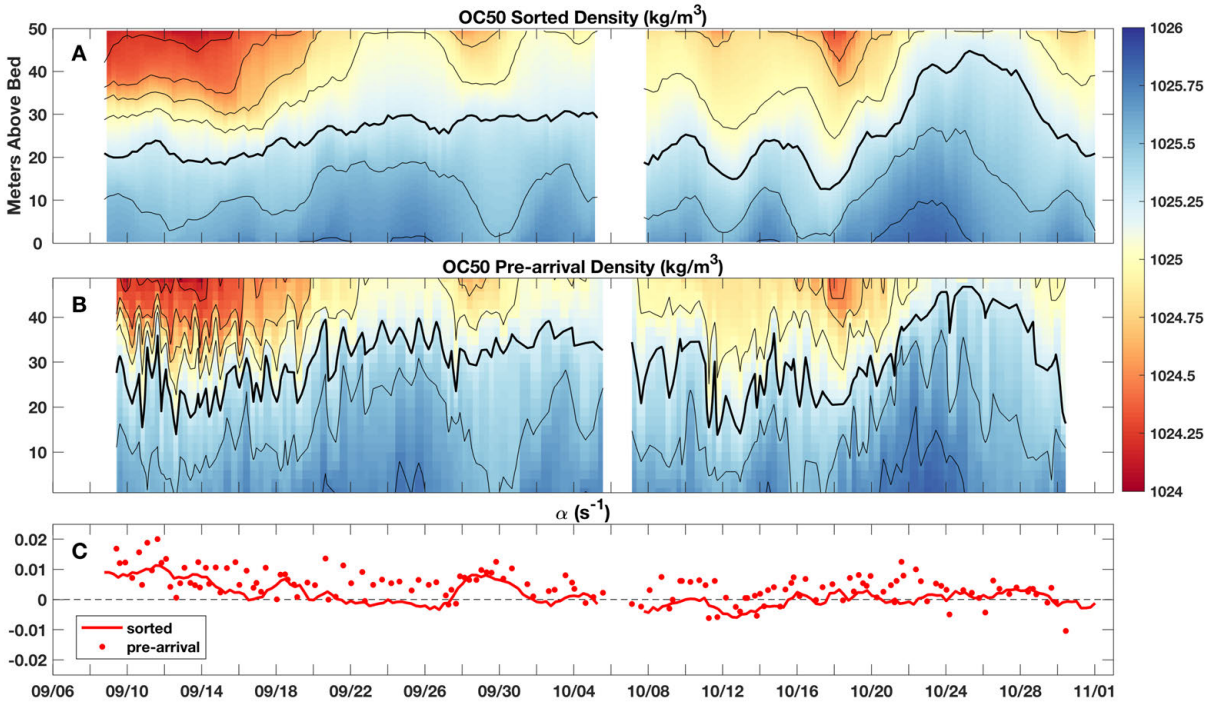


Figure 8. Comparison of sorted (A) and pre-arrival (B) density (kg/m$^3$) for OC50. The contours denote 0.25 kg/m$^3$ isopycnal intervals and the bold contour is the 1025.25 kg/m$^3$ isopycnal. The gap in panel B denotes when the mooring was out of the water. We lose data on the edges of the sorted density due to the sorting method, which is why the gap is wider in A than B. C) Corresponding $\alpha$ (s$^{-1}$)estimates from the sorted (line) and pre-arrival (dot) densities at OC50 (section 2.b.1).

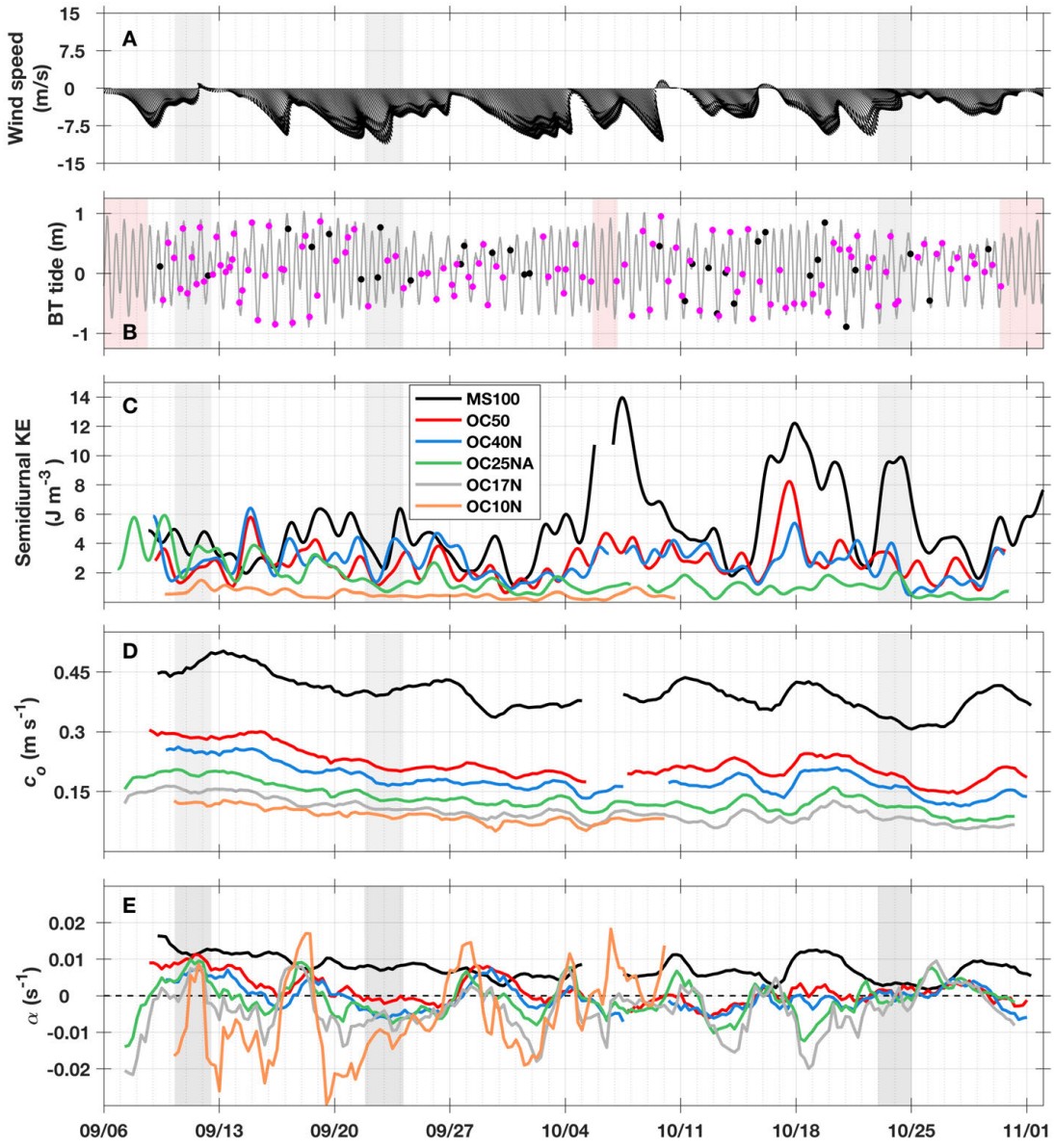


Figure 9. A) Low-passed (>33hrs) winds from the Santa Maria buoy offshore of the Oceano mooring array. Wind direction shown is the direction the wind is blowing towards. B) The barotropic tide and arrival times of internal bores at MS100 (all dots). Magenta dots indicate bores that can be tracked all the way to OC17N. C) Depth-averaged kinetic energy ( $\overline{KE}$ ) in the semidiurnal band (1hr-16h bandpass filtered) for the cross-shore moorings with available velocity data. For this panel only, the blue line is OC40S not OC40N. We present OC40S data

because the semidiurnal $\overline{KE}$ at the two 40m moorings is strongly correlated but the southern location had a longer timeseries of velocity data. D-E) The non-rotating longwave linear phase speed of the bores (D) and α (E) at MS100 (black), OC50 (red), OC40N (blue), OC25NA (green), OC17N (grey), and OC10N (orange) calculated from the sorted density. The 3 grey-shaded times in all panels indicate representative times when α is positive, negative or near-zero. The red shading in panel B indicates when there wasn't enough mooring data to track bores.

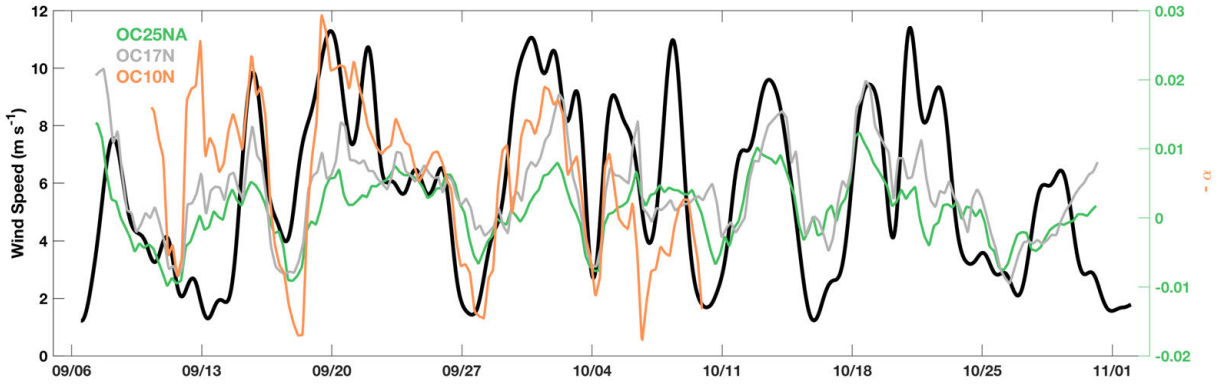


Figure 10. Timeseries of subtidal wind speed (left y-axis, black) and lagged negative α values (right y-axis) at OC25NA (green), OC17N (grey), and OC10N (orange). Lagged correlation coefficients are shown in Table 4.

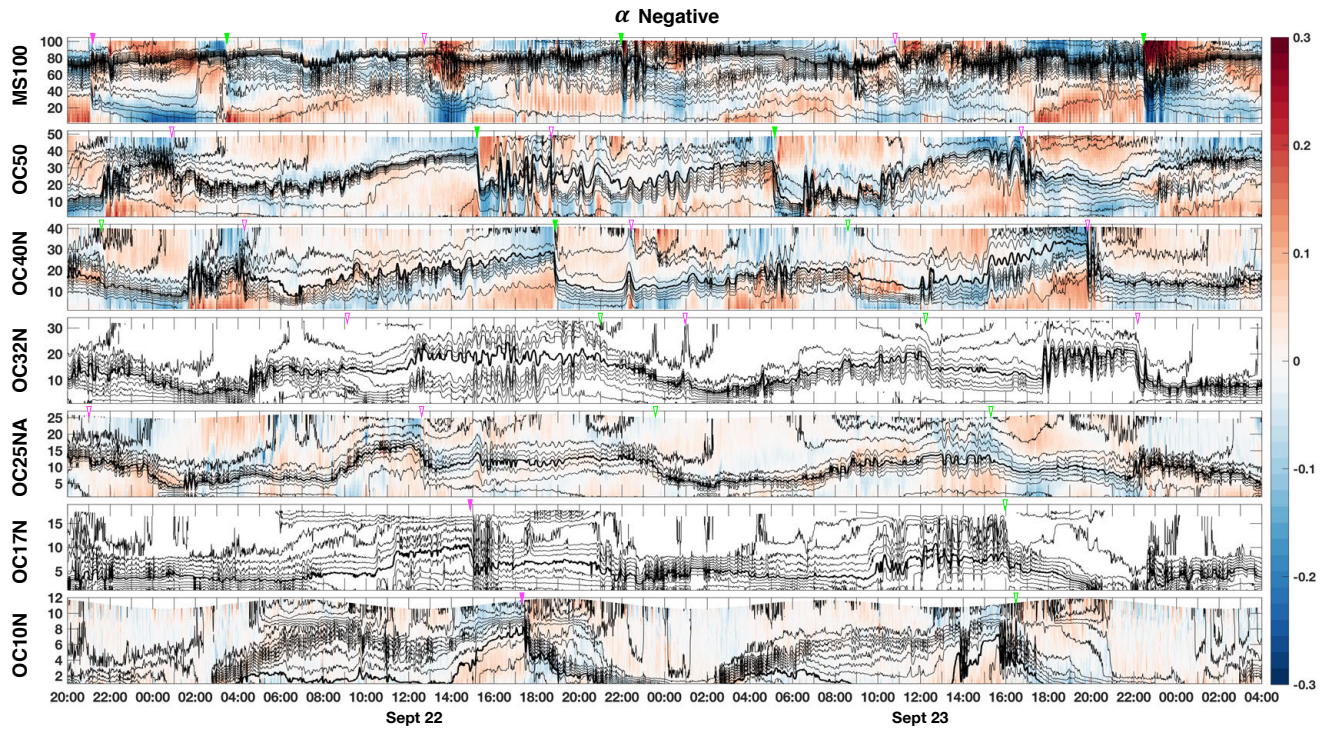


Figure 11. Same as Fig. 5 except for September 21 20:00 – September 24 4:00 (UTC) and 0.25° contours with the 13° isotherm in bold.

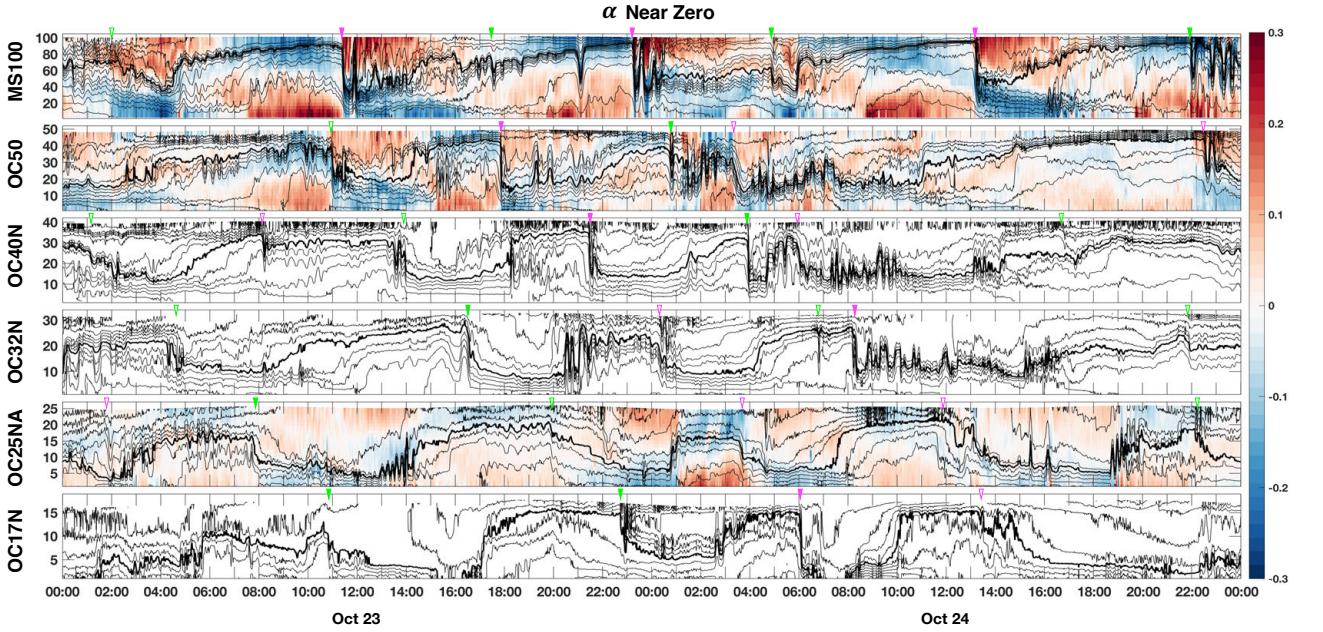


Figure 12. Same as Fig. 5 except for October 23 00:00 – October 24 24:00 (UTC) and 0.25° contours with the 12° isotherm in bold. OC10N was already recovered, so there is no data there.

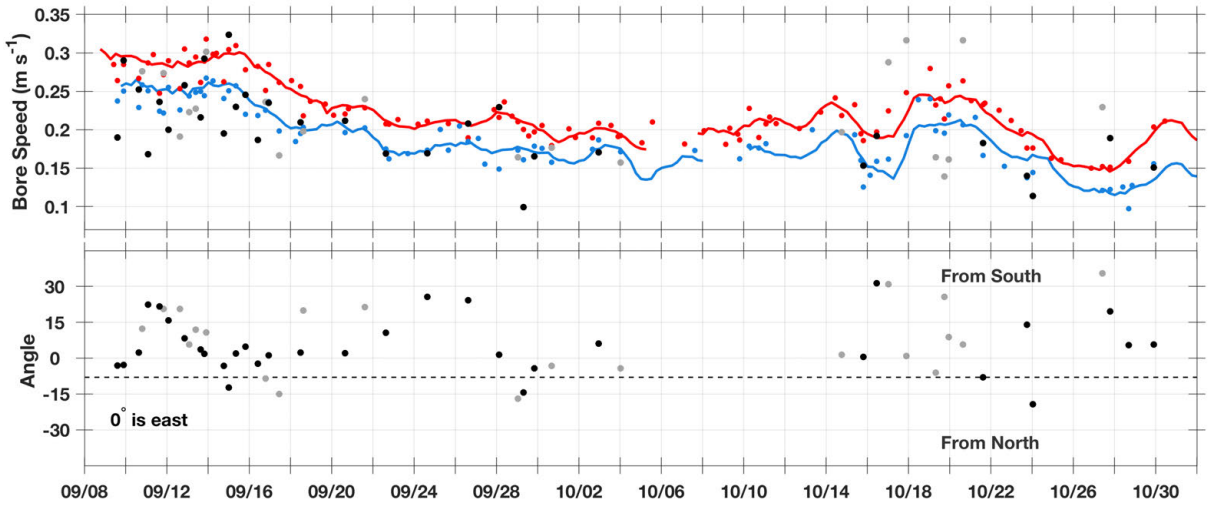


Figure 13. Top) Speeds estimated at triangle A (Fig. 1) from the arrival times at OC50, OC40N, and OC40S (black and grey dots). Black dots indicate tracked bores that meet the +/-7.5min certainty threshold, while grey dots indicate that the +/- 15 min certainty criteria is met. The observed bore speeds are corrected for background currents using the barotropic currents projected in the direction of propagation, with corrections ranging from -0.06 to 0.05 m $s^{-1}$. Nonrotating hydrostatic long-wave linear phase speeds are calculated at OC50 (red) and OC40N (blue) moorings from the sorted (colored lines) and the pre-arrival (colored dots) densities. Bottom) Propagation direction of bores estimated from triangulation method (section 2.b.3) from triangle A. 0° is due east, positive values indicating northward propagation), and the black dashed line indicates the approximate shore-normal direction (-8°).

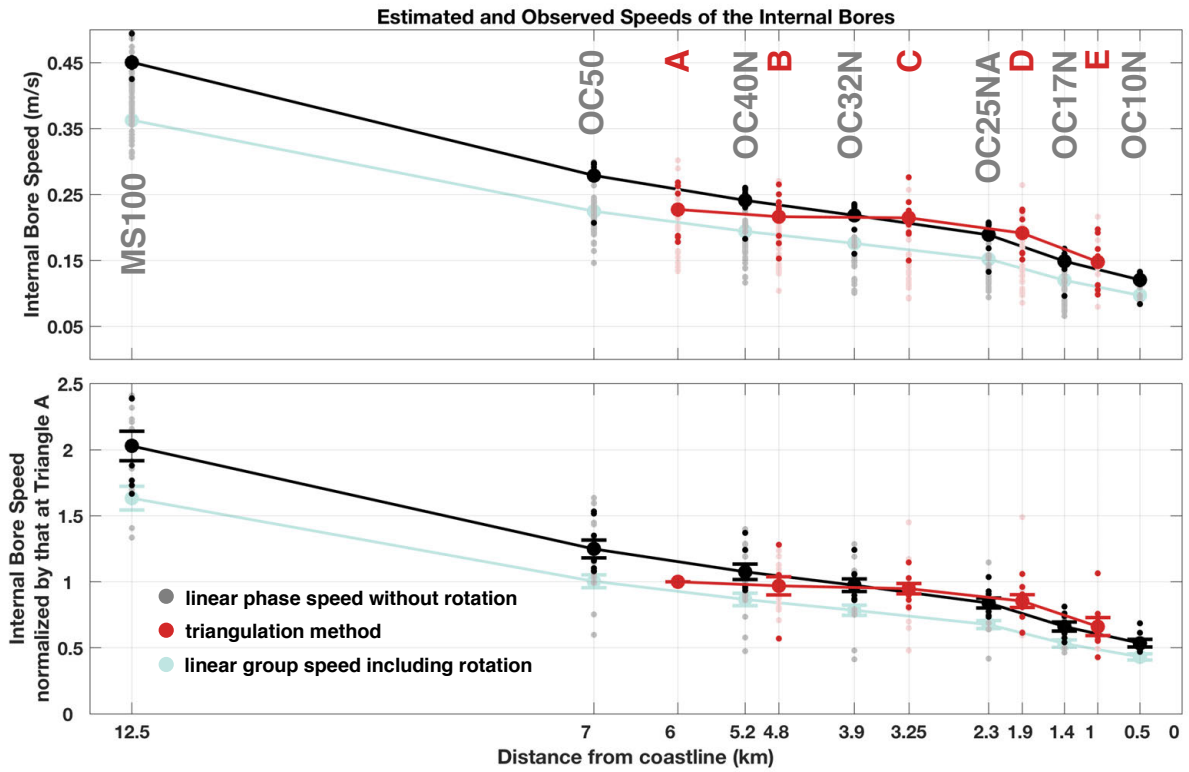


Figure 14. Top) Nonrotating hydrostatic long-wave linear phase speeds ($c_o$) estimated from the sorted density at northern mooring line (grey/black), group velocities for the rotating case with an $M_2$ frequency ($c_g$) estimated from the same moorings (light green), and observed bores speeds calculated from the triangulation method (red) as a function of cross-shore distance. Only estimates for bores that are flagged by the +/-7.5 min certainty threshold are included (smaller light dots, excluding $c_g$), so the number of data points varies at each cross-shore location. Small dark dots indicate the 8 instances when there is a speed estimate at all triangle/rectangle locations (Fig. 1). The average of these 8 cases is shown by larger dark dots. We only show the averages for $c_g$ just to simplify the figure. Bottom) Same as top but all speeds are normalized by the speed at triangle A (6 km). The horizontal lines indicate +/- 1 standard error for the 8 bores tracked with +/-7.5min certainty at each triangle/rectangle location. The across-shelf distance is measured from green dot in Fig. 1.